Label-free Photothermal Quantitative Phase Imaging with Spectral Modulation Interferometry

Joseph G. Thomas

Thesis submitted to the Faculty of the

Virginia Polytechnic Institute and State University

in partial fulfillment of the requirements for the degree of

Master of Science

in

Electrical Engineering

Yizheng Zhu, Chair

Ting-Chung Poon

Wei Zhou

December 9, 2020

Blacksburg, Virginia

Keywords: Phase microscopy, biomedical imaging, interferometry, spectroscopy, photothermal

Label-free Photothermal Quantitative Phase Imaging with Spectral Modulation Interferometry

Joseph G. Thomas

(ABSTRACT)

The photothermal effect is a way in which chemical contrast can be measured as an optical pathlength or phase change. When a chemical species in a sample absorbs optical energy at a particular wavelength, this absorption raises the temperature at these points in the sample via the photothermal effect. This temperature change changes the local refractive index in the sample. Quantitative phase imaging is an interferometric technique for measuring the optical pathlength of sample features. Quantitative phase imaging is capable of detecting the photothermally-induced refractive index change, and is thus a powerful method for performing photothermal imaging. In this work, a thermal wave model is derived from Fourier's law of conduction in conjunction with a medium's heat capacity to derive the diffusion of temperature in a medium. This diffusion theory is transformed to a thermal wave model by applying a temporally modulated thermal source. Analytical expressions for the temperature field surrounding such a modulated thermal source are derived in multiple dimensions. The thermal wave equation is also simulated using a custom finite difference numerical method, and the simulated results are compared to the theoretical expressions with good agreement. The experimental apparatus for inducing such a thermal point source in a medium of water is described using the quantitative phase imaging system of spectral modulation interferometry. The spectral modulation interferometry system is aligned with a visible light pumping laser in two configurations for point source measurement and cell imaging. Label-free chemical imaging is then performed by pumping a field of cellular samples with wide-field

illumination, and the resulting photothermal signal is detected by temporal analysis of the optical pathlength changes, generating the two-dimensional photothermal image. The measured photothermal cell image is qualitatively compared to predicted photothermal image based on the application of the thermal wave model in the spatial frequency domain. The chemical specificity of this technique is also verified by simultaneously pumping absorbing and non-absorbing biological cells in the same field-of-view.

Label-free Photothermal Quantitative Phase Imaging with Spectral Modulation Interferometry

Joseph G. Thomas

(GENERAL AUDIENCE ABSTRACT)

Generating image contrast is a fundamental challenge in optical microscopy. Samples of interest in optical microscopy typically do not have visible absorption contrast without modification. A method of contrast that could provide information about a sample's absorption at different optical wavelengths would be useful for characterizing a sample's chemical content. The photothermal effect is an effect in which the small absorption of light by microscopic samples can be detected as a temperature change. With quantitative phase imaging, this temperature change can be measured by detecting the change in optical density of a sample due to its increase in temperature. Thus, quantitative phase imaging can be used to detect the small absorption of light by microscopic samples and generate two-dimensional images with chemical contrast. This work describes the theory of how thermal energy produced by optical absorption diffuses through a sample immersed in water. A thermal wave model is derived theoretically and compared to a custom simulation of the thermal wave physics with strong agreement. This thermal theory is verified with the quantitative phase imaging system used in this work to characterize the photothermal imaging technique. The photothermal imaging method is then applied to cellular samples, which are pumped with green light. The photothermal image is then generated and compared qualitatively to the image predicted by the thermal theory. The chemical imaging ability of the technique is then demonstrated by simultaneous imaging of absorbing and non-absorbing cells.

Dedication

To my parents Gregory and Elise and my sister Emma.

Acknowledgments

This work began as an undergraduate research experience with Dr. Zhu studying the diffusion of heat generated from absorbed optical energy. This work has been interspersed with other project work in optical coherence tomorgraphy, low cost machine vision for quality control, and photothermal spectroscopy experiments for industrial applications. These last three years, one as an undergraduate and two as a master's student, have been a period of immense technical and personal growth for me. Throughout all of these experiences, I have had the pleasure of working with some fantastic colleagues, and I would thank them here: Dr. Chengshuai Li, Dr. Shichao Chen, Jacob Black, Guannan Shi, Jun Xiao, Xu Su, Shubham Dawda, Dr. Zhixing He, Dr. Ziang Feng, Logan Theis, Eben Fanijo, Kandace Donaldson, Alyssa Huntington, Dr. Alex Brand, and Dr. Rafaella De Vita. I also thank my committee members Dr. Ting-Chung Poon and Dr. Wei Zhou. I would also like to thank my advsior Dr. Yizheng Zhu for many years of discussion, coursework, and learning. I would also like to thank the Bradley Department of Electrical and Computer Engineering for their financial support through the Harry Lynde Bradley Masters Fellowship that partially supported my education and this research work.

Contents

List of Figures

Chapter 1

Introduction

1.1 Imaging

An *image* refers to a recorded set of values that can be mapped to positions in the field of a subject. The defining feature of an image is that a one-to-one mapping exists between image points and points in the sample field.

In optical imaging, this mapping is made through the traditional image formation ability of refractive optical elements that counteract the diffraction of optical waves scattered by the sample to an observation plane [4]. Other schemes exist, such as spectral encoding [5] which maintains this mapping through singlemode fiber. In optical coherence tomography, the mapping can be made over the depth dimension of the sample to provide three-dimensional information of a volumetric sample [6].

The parameter measured across the domain of the sample, be it in one, two, or even three dimensions, is referred to as the *contrast* of the image. For brightfield, or intensity-based, image contrast, the points in the image field contrast from one another based on the variation of optical energy measured for each of these points. This contrast can be produced for multiple wavelengths, such as red, green, and blue for photographic imaging, or even a continuous band of wavelengths for hyperspectral imaging [7].

1.2 Contrast in Optical Microscopy

For samples through which the interrogation via a light field does not provide enough contrast in the recorded optical intensity, a different method of contrast is necessary. One method of contrast particularly powerful for visualizing these samples such as biological cells is *phase* contrast [8]. The phase of an incoming light field will be delayed, relative to some reference wavefront, by the propagation through the sample. In quantitative phase imaging, the phase or optical pathlength of the sample at each point in the image can be measured numerically.

Other methods of contrast exist to provide different information about the sample of interest. In optical microscopy, contrast agents can be broken into two categories: exogenous and endogenous contrast. *Exogenous* contrast refers to the use of labels to generate contrast not inherent to the sample itself. Some popular labels in optical microscopy are fluorophores [9, 10] and nanoparticles [11]. *Endogenous* contrast refers to the interrogation of the sample via one of its inherent properties, such as refractive index [12], absorption, or other chemical or physical properties. Phase contrast is endogenous to the sample, and thus requires no external labeling, which is advantageous for the interrogation of live cells. However, phase contrast cannot provide information about the cells' chemical makeup.

1.3 Photothermal Spectroscopy

Many biological cells contain chemical species important to their function and structure [13]. These chemical species often have wavelengths or bands of wavelengths in which they heavily absorb optical energy. In other regions of the electromagnetic spectrum, they are transparent. A method of imaging that would provide quantitative information about the absorption of different wavelengths by a sample would then be highly useful for interrogating the chemical

makeup of these samples. This work describes the development of such a technique, which is capable of providing chemical contrast imaging of unlabeled live biological cells.

The photothermal (PT) effect refers to the conversion of absorbed optical energy to heat [14]. This absorption raises the temperature of the sample in the area surrounding the absorption point. Thus, if this temperature change can be measured, the absorption properties of a sample can be interrogated. To facilitate the detection of this effect, the photothermal source is typically modulated, and the resulting temperature distribution takes the form of a thermal wave.

A particularly important secondary effect of the photothermal temperature increase is that of the *thermo-optic effect*. The thermo-optic effect describes the change in refractive index of a medium due to a temperature change. This value is typically negative, as an increase in temperature will produce a decrease in the optical density of a material. For a linear model of refractive index as a function of temperature, the thermo-optic coefficient describes the derivative of refractive index with respect to temperature. For a small temperature change, the refractive index change can be described as

$$\Delta n = \frac{dn}{dT}\Delta T, \tag{1.1}$$

where $\frac{dn}{dT}$ is the thermo-optic coefficient for the material. For water, the thermo-optic coefficient is approximately $-1.1 \times 10^{-4}\frac{1}{K}$ [15].

The usage of the photothermal effect to perform both absorption spectroscopy as well as absorption contrast imaging has a long history in the scientific literature. Multiple books have documented the advancements of photothermal spectroscopy and the underlying heat diffusion theory, beginning with a single point measurement of a bulk material and advancing to two-dimensional and even three-dimensional imaging [14, 16, 17]. The theory of a

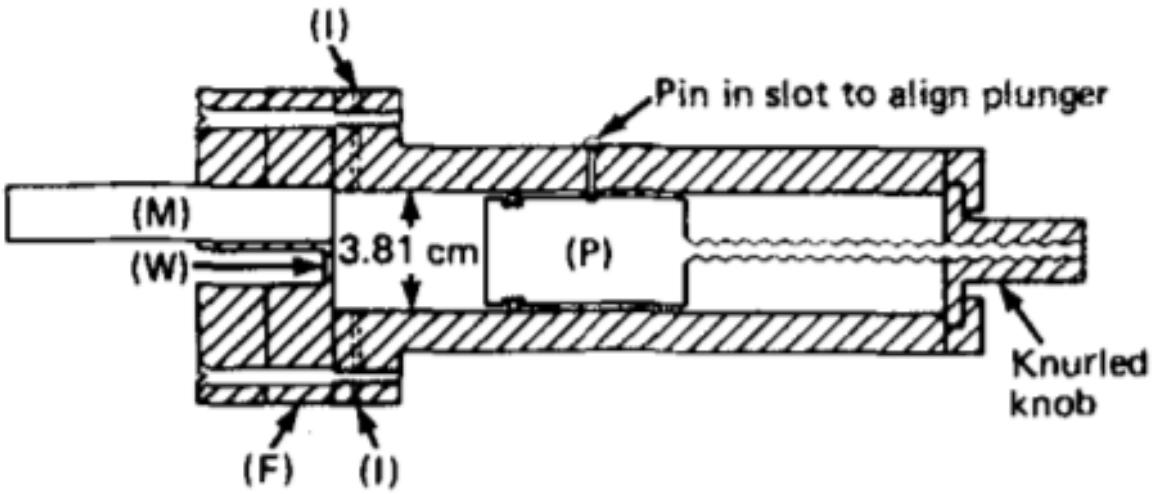

Fig. 1.1. *Size considerations in the design of cells for photoacoustic spectroscopy* [1], reproduced under fair use. (W) denotes the window for optical pumping and (M) the microphone.

photothermally generated signal was first described in the context of an acoustic probe [18]. These early efforts used acoustic transducers to measure the pressure changes in a gas in close thermal contact with the absorbing sample [1]. Photoacoustic detection of the photothermal signal has the advantage of simple detector, as an acoustic transducer can be used to detect the signal. Constraints of this method require the sample to be enclosed in an acoustic cell, and the resulting signal is sensitive to the geometry of such a cell as in Figure 1.1. This configuration is suitable for spectroscopic purposes of bulk liquids and gases, but for solid materials, as well as samples of interest in imaging, a more flexible approach is required.

A photothermal spectroscopy configuration suitable for solids is that of the "mirage effect" shown in Figure 1.2. The bulk solid sample is pumped with a modulated optical source, and the thermal wave transferred to the air above the sample deflects the horizontally aligned probe beam [2]. The configuration in Figure 1.2 is also suitable for *imaging* solid samples. Photothermal imaging of subsurface structures in a solid sample was performed using this all-optical, beam deflection approach. In this configuration, the photothermal wave is allowed

to propagate from its source at the subsurface features of a solid into the ambient air through which a probe beam is aligned. The deflection of the probe beam due to refractive index changes from the thermal wave is then measured with a photodiode [19]. Scanning the sample produced two-dimensional images.

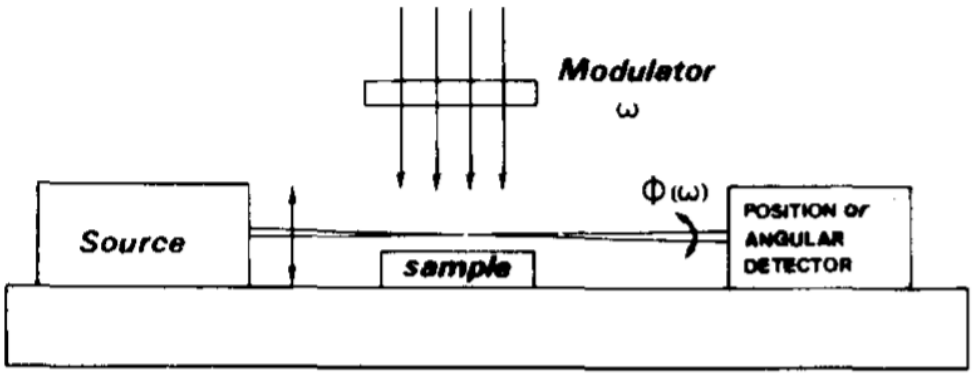

Fig. 1.2. *Thermo-optical spectroscopy: Detection by the "mirage effect"* [2], reproduced under fair use.

Another all-optical approach for measuring the photothermal signal is that of modulated optical reflectance [14]. In this technique, the photothermally-induced refractive index change is directly measured via a change in the optical reflection coefficient of the sample surface [20].

With a phase sensitive technique, the refractive variation of a sample can be measured directly and quantitatively via the phase delay of a light field rather than through beam deflection. Therefore, the refractive index change produced from the photothermal effect is a perfect candidate for interferometric detection.

The first efforts in using photo-generated heat as a method of microscope image contrast began with nanoparticle labels. As an alternative to fluorescent labelled samples, nanopar-

ticles can generate a highly tuned resonant absorption and experience no photobleaching [21]. Thus, these particles were a useful candidate for preliminary photothermal implementations. At high modulation frequencies, the thermal profile of surrounding the nanoparticle has a large gradient and acts as a thermal lens. The scattering by this thermal lens can be measured and used to generate the photothermal amplitude by scanning across sample points [22]. Later experiments extended this ability to act as a label by tagging cells with the absorbing particles [23]. These early investigations into the photothermal method of image contrast used high modulation frequencies, for which the temperature distribution varies quickly spatially, to create a thermal lens. The sample stage was then scanned laterally across the coincident pump and probe beams to generate a two-dimensional image. This method of signal acquisition and generation has multiple drawbacks compared to wide-field photothermal signal acquisition. First, the detection of the PT signal by the thermal lens scattering requires a very high modulation frequency to produce such a spatially varying temperature distribution. Based on the photothermal theory derived in later sections of this work, it is evident that the photothermal signal amplitude decreases with increasing modulation frequency. Thus, a sensing method that does not rely on creating such a large temperature variation could use lower modulation frequencies which produce a larger temperature variation. Furthermore, the scattering of the probe beam by the thermal lens requires coincident pump and probe beams. Thus, the two must share the same focusing optics. This constraint restricts the choice of pump wavelengths to ones that can be effectively focused by the typically visible or near-infrared optics used in the sensing or microscope system. For pumping the sample with vastly different wavelengths, such as the mid-infrared region in which many biological cells contain chemicals of interest, a different pump and probe geometry is required. Finally, the scanning of the sample stage dramatically reduces the imaging rate of the photothermal microscope.

Current efforts have moved away from the thermal-lens method of signal generation and acquisition, and have used a variety of wide-field imaging schemes to eliminate the disadvantages described above. Most of these implementations are interferometric in nature, as the phase-sensitive interference signal allows sensitive detection of the photothermally-induced refractive index change. Transition works between these two methods have used a variety of interferometric implementations with high success. Hartmann wavefront sensors have been used to measure a hot and cold frame [24], and calculate the difference to produce the photothermal signal.

1.4 Quantitative Phase Imaging

As discussed previously, the photothermal effect can be detected in a variety of schemes. The effect most suited to widefield photothermal imaging, in which the entire sample is pumped simultaneously and imaged simultaneously or near-simultaneously, is that of a phase-sensitive recording technique. In particular, quantitative phase imaging (QPI) allows the precise measurement of the optical phase delay induced by the photothermal effect.

The QPI system used in this work is Spectral Modulation Interferometry (SMI) [3]. SMI, shown in Figure 1.3, is a specific form of spectral interferometry that uses spectral encoding for fast acquisition of phase images. In SMI, a broadband light source is dispersed spatially using a diffraction grating, and the spectrum of wavelengths is mapped to a line of positions in the image plane. Scanning this line with a galvonometric mirror and synchronizing the linescan camera exposure allows the buildup of two-dimensional images.

SMI produces speckle-free quantitative phase images with high speed and high sensitivity. Figure 1.4 displays phase images recorded with SMI, displayed in color based on measured optical pathlength and rendered with lighting. The speckle-free nature of these images is

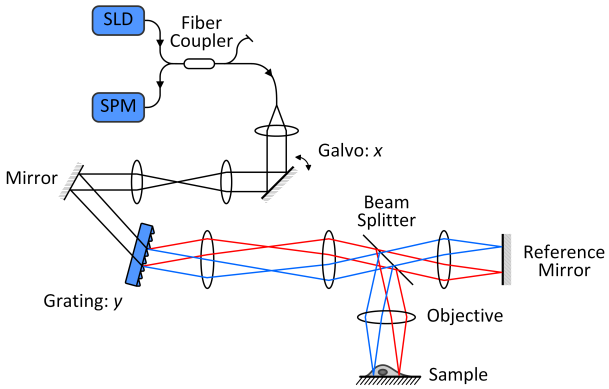

Fig. 1.3. Spectral Modulation Interferometry [3], reproduced with permission.

visible, as well as the high SNR resulting from SMI's 0.1 nm temporal sensitivity.

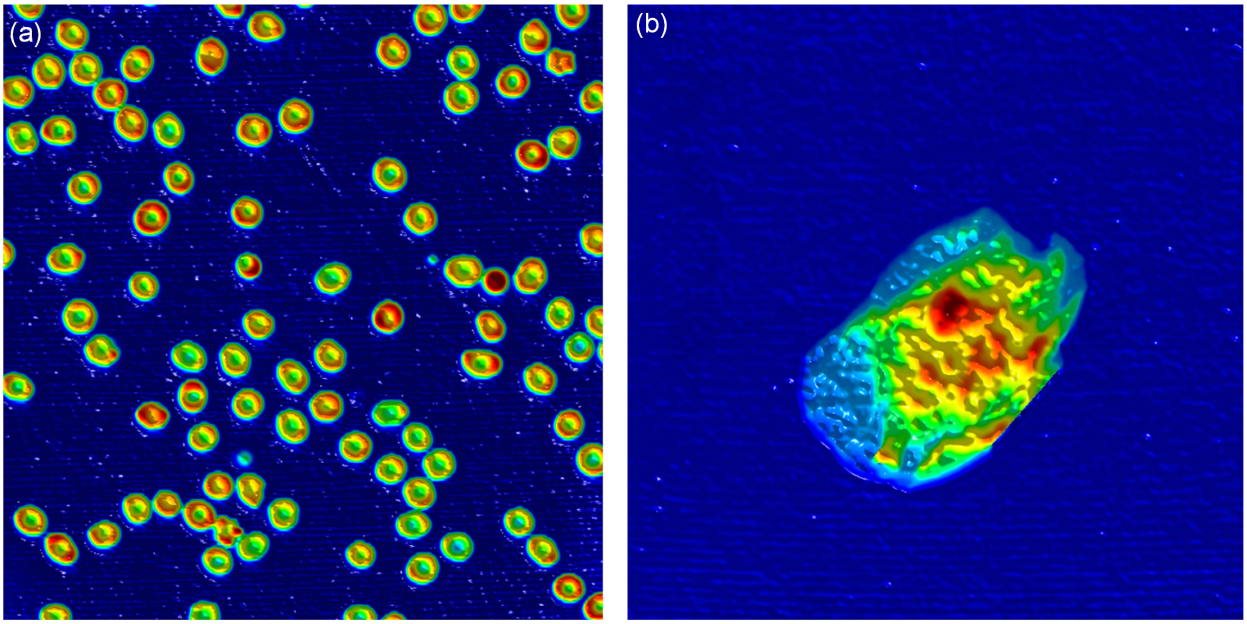

Fig. 1.4. Quantitative phase images captured with SMI: red blood cells (a) and cheek cell (b).

The QPI system used in this work is based on the Michelson interferometer architecture. In this configuration, the microscope operates in reflection mode. As seen in Figure 1.5, a beamsplitter splits an incident light wave into two wavefronts, typically of near equal intensity. One wavefront travels through the sample, while the other is reflected by a flat

mirror. The flat wavefront reflected by the mirror is used as a phase reference, while each point on the sample wavefront undergoes a phase delay by the sample relative to the reference wavefront.

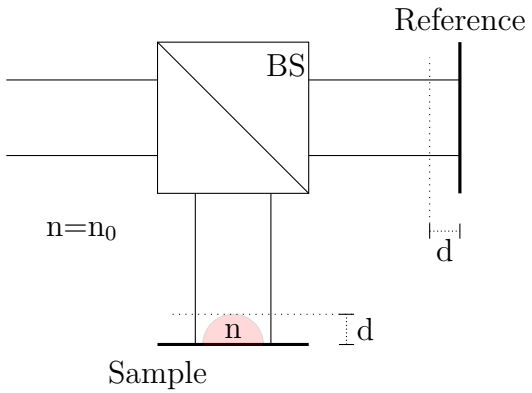

Fig. 1.5. Michelson interferometer.

In spectral interferometry, the problem of optical pathlength estimation can be transformed to one of frequency and phase estimation in the frequency domain. The sample and reference wavefronts are identical after the beamsplitter. The reference wavefront has an optical pathlength after the beamsplitter of $OPL = L_r$. The sample wavefront has the sample initial optical pathlength L_s, but accumulates additional phase as it propagates through the sample with refractive index $n(x, y)$. Thus, the sample wavefront after the beamsplitter experiences optical pathlength $OPL = L_s + (n(x, y) - n_0)d(x, y)$, where $d(x, y)$ is the physical sample thickness, and n_0 is the refractive index of the medium in which the sample is immersed.

The total field on the spectrometer can then be written, with the accumulated double-pass OPL from each arm, as

$$E_{tot} = E_s + E_r = E_s(x, y)e^{j2k(L_s+(n(x,y)-n_0)d(x,y))} + E_r e^{j2kL_r}. \tag{1.2}$$

The signal detected by the spectrometer CCD is then

$$I_{tot} = E_{tot}E_{tot}^{*} = (E_s(x,y)e^{j2k(L_s+(n(x,y)-n_0)d(x,y))}+E_re^{j2kL_r})(E_s(x,y)e^{-j2k(L_s+(n(x,y)-n_0)d(x,y))}+E_re^{-j2kL_r}). \tag{1.3}$$

The intensity signal is then

$$I_{tot}(x,y) = E_s(x,y)^2 + E_r^2 + 2E_rE_s(x,y)cos(2k[(n(x,y)-n_0)d(x,y)] + 2kL_0), \tag{1.4}$$

where $L_0 = L_s - L_r$.

The interferogram written up to this point is the most general form signal model for the Michelson interferometer. In spectral interferometry, the wavenumber term in Equation 1.4 is a vector of wavenumbers sampled by the spectrometer, and the optical pathlength can be determined by extracting the frequency and phase of the sinusoid term with Fourier analysis.

The signal model of SMI is similar to that of spectral interferometry described above. However, the sampled vector of wavenumbers now has a spatial dependence, $k(y) = k_0 + \alpha y$, where k_0 is the lowest sampled wavenumber, α is the spatial dispersion coefficient in the image plane [$\mathrm{nm\,\mu m^{-1}}$], and y [µm] is the spatial position in the image plane. With this adjustment input into Equation 1.4, the resulting interference pattern is

$$I_{tot}(x,y) = E_s(x,y)^2 + E_r^2 + 2E_rE_s(x,y)cos(2(k_0+\alpha y)[(n(x,y)-n_0)d(x,y)] + 2(k_0+\alpha y)L_0). \tag{1.5}$$

Rearranging Equation 1.5,

$$I_{tot}(x,y) = E_s(x,y)^2+E_r^2+2E_rE_s(x,y)cos(2k_0[(n(x,y)-n_0)d(x,y)+L_0]+2\alpha y[(n(x,y)-n_0)d(x,y)+L_0]). \tag{1.6}$$

Equation 1.6 can be seen as a phase or frequency modulation scheme. For typical cellular

samples and interferometer arm separations, $L_0 >> (n(x,y) - n_0)d(x,y)$, and L_0 acts as a carrier frequency and sets the initial or background phase of the phase image. The sample phase and carrier frequency shift (depending on the spatial extent of the sample) are then determined by the sample itself.

To extract the sample optical pathlength, the phase of the analytic signal of Equation 1.6, the modulated signal centered at $2\alpha y[(n(x,y) - n_0)d(x,y) + L_0]$ is bandpass filtered. The signal is then downshifted to be centered at baseband by multiplication of the appropriate carrier signal. The phase of this signal is then extracted by taking the angle of this final analytic signal. This phase signal contains an initial component set by L_0 which can be subtracted to leave only the sample optical pathlength, $(n(x,y) - n_0)d(x,y)$.

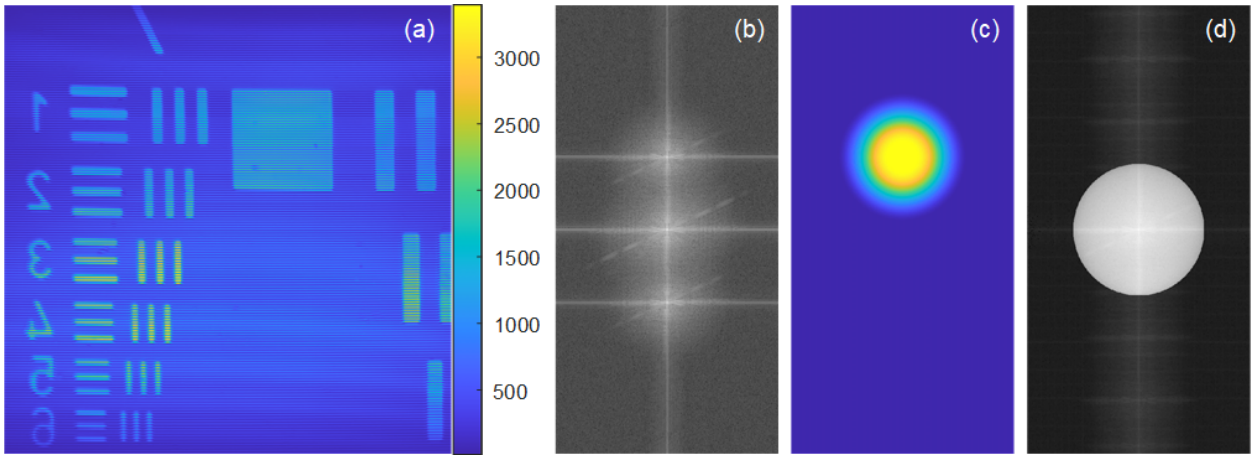

Fig. 1.6. SMI intensity: Interferogram (a), 2D FFT of interference signal (b), filter (c), downshifted signal (d).

Figure 1.6 shows the first four steps of the SMI phase extraction procedure. Figure 1.6(a) shows the interferogram generated by directly recording the interferences of the wavelengths sampled by the spectrometer in Equation 1.6. The spectral direction is the vertical image axis, in which a sinusoidal intensity is visible. The scanning direction is the horizontal axis, in which there is no interference signal. Figure 1.6(b) shows the two-dimensional discrete Fourier transform in log scale. The double-band signal described by the phase modulation

scheme in Equation 1.6 is separated from baseband. Filtering one of the modulated analytic signals and multiplication with a complex exponential at the carrier frequency shifts the modulated signal back to baseband in Figure 1.6(d).

Upon isolating the modulated signal and shifting to baseband, the wrapped phase image, Figure 1.7(a), is extracted by taking the phase of the baseband signal. Performing two-dimensional phase unwrapping with the Goldstein algorithm yields Figure 1.7(b). Conversion from the phase delay to the optical pathlength by multiplication by the appropriate wavelength for each vertical pixel produces Figure 1.7(c). Finally, the slow-varying OPL background is removed by fitting and removing the Zernike polynomials to create Figure 1.7(d).

This encoding scheme sacrifices the absolute OPL estimation of spectral interferometry, in which the entire source spectrum is used to make an absolute OPL estimation at a single image point [25]. However, the spectral encoding scheme trades absolute OPL measurement for the simultaneous imaging of a line of image points for which OPL (or phase) relative to the reference wavefront is measured. This tradeoff to capture images by one-dimensionally scanning an imaging line allows the SMI system to acquire two-dimensional phase images with high speed, as the acquisition time is reduced by a factor of one dimension of the image resolution when compared to two-dimensional point scanning.

SMI also eliminates the sensitivity-reducing effect of coherent speckle in the image plane compared to other coherent imaging schemes. As the source spectrum is dispersed spatially in the image plane, the spatial coherence of points in the image plane is reduced, such that the only points in the image plane close enough to be coherent are below the optical resolution of the system, and the speckle is eliminated.

The linescan nature of SMI also allows a variable scanning rate and resolution in one di-

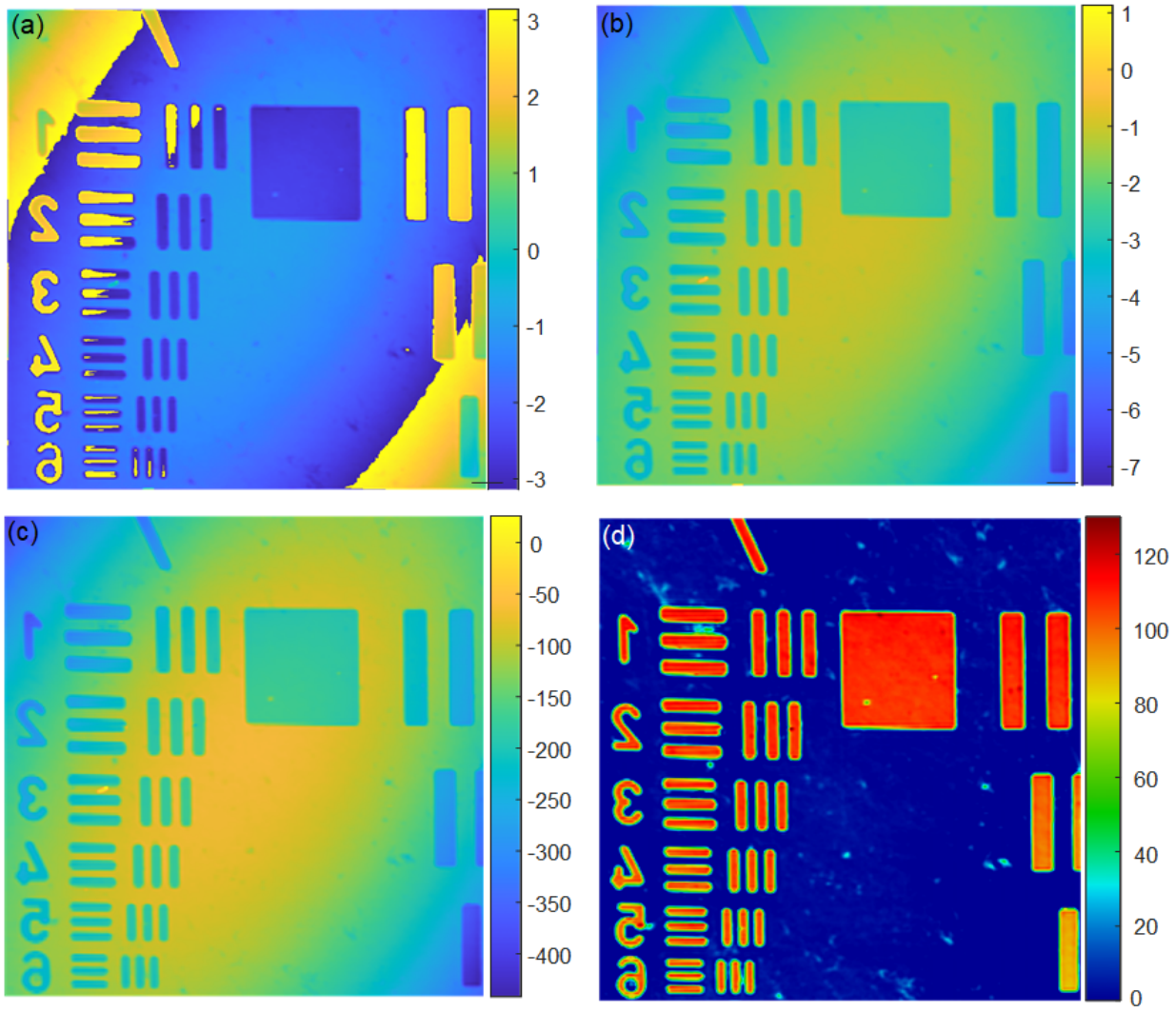

Fig. 1.7. SMI phase: Wrapped phase [rad] (a), unwrapped phase [rad] (b), raw optical pathlength [nm] (c), background-subtracted optical pathlength [nm] (d)

mension. The scanning galvonometric mirror can be operated from DC voltage, in which the SMI system samples a stationary line at the full readout rate of the spectrometer, up to a scan rate of 120 Hz with 512 sampled lines across the field-of-view. Thus, depending on the necessary field-of-view, image resolution, and sampling rate, the SMI system can be adjusted for best performance.

Due to the modulated nature of the photothermal signal induced, the QPI scheme must have

high resolving ability in the temporal domain. This ability is achieved by meeting constraints in two parameters of traditional imaging. The most basic parameter for visualizing signals with short temporal extent is the exposure time of the phase imaging system. Consider a 1 kHz sinusoidal refractive index change in the measured signal. This refractive index change will change the measured optical pathlength proportionally. Thus, to track this signal, the exposure time of the QPI system must be low compared to the period of the modulation, so that significant reduction of signal energy does not occur. Consider a camera exposure time of 1 ms. Assume the exposure and signal waveforms are synchronized to begin at the same time. As the camera is exposed over the entire period of modulation, the sampled phase value of this exposure will be an average value of the signal over this time. In the modulated case, this average becomes near zero. Thus, it is clear that to resolve a sinusoidal photothermal change, system exposure times need to be on the order of one-tenth the period of modulation or lower to avoid the averaging effect that will reduce measured signal energy.

Another fundamental parameter for resolving these induced modulated signals is that of the QPI system imaging rate. The Nyquist-Shannon Theorem states that to resolve a sinusoid after sampling, the sampling rate must be twice or more than the sinusoid frequency. This criterion is indeed the case in order to resolve the sinusoid in the time domain. However, if the exposure time meets the requirements outlined in the previous paragraph, a zero-bandwith sinusoidal signal can be undersampled without loss of the signal amplitude or phase information. This technique is referred to as *bandpass sampling*, and requires that the imaging rate be greater than twice the bandwidth of the signal of interest. This finer point is of key interest in our sensing of the photothermal signal, as it relaxes the requirement of fast imaging rate compared to the modulation frequency, as long as the exposure time is kept below the modulation period.

A chief parameter for resolving the photothermal image with adequate signal-to-noise ratio

is the sensitivity of the phase imaging system. This sensitivity is defined as the standard deviation of the optical pathlength for a large array of temporal samples under static conditions. As the photothermal amplitude image is generated by extracting the amplitude of the fundamental frequency of the pumping modulation, the SNR of the final image is the ratio of this amplitude to the amplitude floor of the SMI system at this frequency. Thus, a QPI system with a high sensitivity, particularly one whith a low noise floor in a useful band of its sampling spectrum, will increase the photothermal image SNR.

Chapter 2

Photothermal Theory

To describe the temperature distribution around a modulated thermal source, the theory of heat diffusion within a medium is derived from Fourier's Law of Conduction as well as the heat capacity of a material, and an implementation of a finite difference numerical simulation confirms the analytical solutions of interest.

2.1 Fourier's Law of Conduction

The conduction of thermal energy is governed by Fourier's Law of Conduction [17],

$$\vec{q} = -K\nabla T, \tag{2.1}$$

where f is the heat flux density $[\frac{W}{m^2}]$, K is the thermal conductivity of the material $[\frac{W}{mK}]$, and T is the scalar temperature field $[K]$ [17].

It can be seen in Equation 2.1 that for a scalar temperature field, the flow of heat is a vector field in the direction of high to low temperature.

2.2 Specific Heat Capacity

The manner in which a material changes temperature based on the addition or subtraction of thermal energy is governed by its heat capacity. Extending this idea to a homogeneous mate-

rial, the *specific* heat capacity can be described as the heat capacity density. Given a change in thermal energy dQ $[J]$ in an infinitesimal volume dV $[m^3]$, the change in temperature is described by

$$\Delta T = \frac{\Delta Q}{\rho c}, \tag{2.2}$$

where ΔQ is the change in thermal energy of the body, ρ $[\frac{kg}{m^3}]$ is the volumetric mass density of the material, c $[\frac{J}{kgK}]$ is the specific heat capacity of the material, and ΔT $[K]$ is the resulting temperature change.

2.3 Heat Equation

Consider a volumetric region in a homogeneous material with material parameters m, c, and K. We consider the addition to this region of some thermal energy ΔE, the loss of some thermal energy due to conduction as ΔQ, and some thermal energy going to the increase in temperature. We apply conservation of energy to this region and write

$$\Delta E - \Delta Q = mc\Delta T. \tag{2.3}$$

Qualitatively, Equation 2.3 describes that any change of thermal energy to the region manifests as a temperature change of the region.

We consider this temperature change over a short time period Δt, and describe the rate of temperature change based on the thermal power added or subtracted from the region

$$\frac{\Delta E}{\Delta t} - \frac{\Delta Q}{\Delta t} = mc\frac{\Delta T}{\Delta t} \tag{2.4}$$

We then take this time period to be infinitesimally short by applying the limit $\lim_{\Delta t \to 0}$ to

describe the instantaneous rate of temperature change

$$\frac{dE}{dt} - \frac{dQ}{dt} = mc\frac{dT}{dt}. \tag{2.5}$$

We rewrite the addition of thermal power to the medium as a thermal source $P = \frac{dE}{dt}$, and consider the subtraction of thermal energy as the surface summation of flux density out of the volume. We also consider the mass of the region as the volume summation of the mass density

$$P - \oint_S \vec{q} \cdot \vec{ds} = \iiint_V \rho c \frac{dT}{dt} dV. \tag{2.6}$$

We apply the divergence theorem to the outward heat flux density $\vec{q}$ to state that

$$\oint_S \vec{q} \cdot \vec{ds} = \iiint_V \nabla \cdot \vec{q} dV. \tag{2.7}$$

We apply Equation 2.7 to write

$$P - \iiint_V \nabla \cdot \vec{q} dV = \iiint_V \rho c \frac{dT}{dt} dV. \tag{2.8}$$

We then consider the volumetric region to shrink infinitesimally and consider the volume density of the thermal power

$$\lim_{V \to 0} \frac{1}{V} P - \lim_{V \to 0} \frac{1}{V} \iiint_V \nabla \cdot \vec{q} dV = \lim_{V \to 0} \frac{1}{V} \iiint_V \rho c \frac{dT}{dt} dV. \tag{2.9}$$

$$R - \nabla \cdot \vec{q} = \rho c \frac{dT}{dt}. \tag{2.10}$$

We use Fourier's Law of Equation 2.1 to write

$$R - \nabla \cdot (-K\nabla T) = \rho c \frac{dT}{dt}. \tag{2.11}$$

Using the definition of the Laplacian, we also write

$$R + K\nabla^2 T = \rho c \frac{dT}{dt}. \tag{2.12}$$

We finally define the parameter *thermal diffusivity* as $\alpha = \frac{K}{\rho c}$ and write the sourced diffusion equation

$$\alpha \nabla^2 T - \frac{dT}{dt} = \frac{R}{\rho c}. \tag{2.13}$$

For our induced photothermal imaging technique, we only consider temperature variations with sinusoidal dependence. Thus, we assume $T(t) = e^{j\omega t}$, where $\omega = 2\pi f$ and f is the temporal modulation frequency $[Hz]$. We apply separation of variables to the scalar temperature field and and write

$$T(\vec{r}, t) = T(\vec{r})T(t). \tag{2.14}$$

Thus, the simplified time-harmonic version of Equation 2.13 is

$$\alpha \nabla^2 T(\vec{r}) - j\omega T(\vec{r}) = \frac{R}{\rho c}. \tag{2.15}$$

Important to note from Equation 2.15 is that by applying the assumption of a harmonic temperature field, we transform the diffusion equation of Equation 2.13 into the wave equation

$$\nabla^2 T(\vec{r}) - k^2 T(\vec{r}) = \frac{1}{\rho c}\delta(\vec{r}), \tag{2.16}$$

where $k^2 = \frac{j\omega}{\alpha}$.

It can be seen that Equation 2.16 has complex wavenumber

$$k = \sqrt{\frac{j\omega}{\alpha}} = \sqrt{e^{j\frac{\pi}{2}}\frac{\omega}{\alpha}} = e^{j\frac{\pi}{4}}\sqrt{\frac{\omega}{\alpha}} = (1+j)\sqrt{\frac{\omega}{2\alpha}}. \tag{2.17}$$

.

The formulation of Equation 2.17 will prove useful for the free-space Green's function solutions of the harmonic heat equation.

2.3.1 1D Green's Function

In one dimension, we consider the harmonic solution to the one-dimensional formulation, that is $T(\vec{r}) = T(x)$, of the thermal wave equation in Equation 2.16. We also consider the source-free case

$$\frac{\partial^2 T(x)}{\partial x^2} = k^2 T(x). \tag{2.18}$$

The solution of Equation 2.18 is given as

$$T(x) = A_0 e^{kx} + B_0 e^{-kx}. \tag{2.19}$$

With complex $k = (1+j)\sqrt{\frac{\omega}{2\alpha}} = (1+j)\beta$ we have

$$T(x) = A_0 e^{(1+j)\beta x} + B_0 e^{-(1+j)\beta x} \tag{2.20}$$

and

$$T(x) = A_0 e^{j\beta x} e^{\beta x} + B_0 e^{-j\beta x} e^{-\beta x}. \tag{2.21}$$

Based on the domain of $x \in (-\infty, \infty)$, we define the piece-wise physical solution

$$T(x,t) = \begin{cases} A_0 e^{j(\beta x + \omega t)} e^{\beta x} & x \leq 0 \\ B_0 e^{-j(\beta x - \omega t)} e^{-\beta x} & x > 0 \end{cases}. \tag{2.22}$$

With a heat source of $Q = 1[W]$, we apply the divergence theorem at $x = 0$. Each half-region of the space of x receives half of the $1[W]$ source. With only 1D, there is no decrease in the heat-flux density emanating outward from the source. The heat flux density of a temperature distribution is given by the gradient of the temperature by Fourier's law as

$$q = -K\nabla T. \tag{2.23}$$

In our one-dimensional space, Fourier's law for $x = 0^+$ is

$$q = -K\frac{dT}{dx}|_{x=0^+} = \frac{1}{2}. \tag{2.24}$$

Thus,

$$\frac{dT}{dx}|_{x=0^+} = -\frac{1}{2K}. \tag{2.25}$$

Computing the spatial derivative,

$$\frac{dT}{dx}|_{x=0^+} = -B_0(1+j)\beta. \tag{2.26}$$

Applying this boundary condition

$$B_0 = \frac{1}{2K}\frac{1}{\sqrt{2}}e^{-j\frac{\pi}{4}}\frac{1}{\beta}. \tag{2.27}$$

Finally,

$$B_0 = \frac{1}{2K} e^{-j\frac{\pi}{4}} \sqrt{\frac{\alpha}{\omega}}. \tag{2.28}$$

For $x \leq 0$, we reverse the sign of the outward flux, as the direction of heat transfer is encoded by the sign of x, rather than the expression itself. Thus,

$$\frac{1}{2K} = (1+j)\beta, \tag{2.29}$$

and we have $A_0 = B_0$.

Thus the final solution is

$$T(x,t) = \begin{cases} \frac{1}{2K}\sqrt{\frac{\alpha}{\omega}} e^{j(\beta x + \omega t - \frac{\pi}{4})} e^{\beta x} & x \leq 0 \\ \frac{1}{2K}\sqrt{\frac{\alpha}{\omega}} e^{-j(\beta x - \omega t + \frac{\pi}{4})} e^{-\beta x} & x > 0 \end{cases}.$$

2.3.2 2D Green's Function

Applying separation of variables to in 2D, we have

$$T(r,\theta,t) = T(r)T(\theta)T(t). \tag{2.30}$$

Expanding Equation 2.13 with the Laplacian in polar coordinates,

$$\frac{\partial T}{\partial t} = \alpha\left(\frac{\partial^2 T}{\partial r^2} + \frac{1}{r}\frac{\partial T}{\partial r} + \frac{1}{r^2}\frac{\partial^2 T}{\partial \theta^2}\right). \tag{2.31}$$

We apply the radial symmetry of the situation, and take the angular derivative to be zero

$$\frac{\partial T}{\partial t} = \alpha\left(\frac{\partial^2 T}{\partial r^2} + \frac{1}{r}\frac{\partial T}{\partial r}\right). \tag{2.32}$$

Assuming we have a sinusoidal time dependence,

$$e^{j\omega t}\frac{\partial^2 T(r)}{\partial r^2} + e^{j\omega t}\frac{1}{r}\frac{\partial T(r)}{\partial r} = \frac{j\omega}{\alpha}e^{j\omega t}T(r). \tag{2.33}$$

Finally we have the modified cylindrical Bessel equation of order zero

$$r^2\frac{\partial^2 T(r)}{\partial r^2} + r\frac{\partial T(r)}{\partial r} = r^2\frac{j\omega}{\alpha}T(r). \tag{2.34}$$

The solution is then the modified Bessel function of second kind and zero order, with a complex wavenumber

$$T(r,t) = A_0 K_0(kr)e^{j\omega t} \tag{2.35}$$

with $k = \sqrt{\frac{j\omega}{\alpha}}$.

To determine the coefficent of the solution, we apply the information that the heat flux is continuous as we move radially outward from the source. The heat flux is given from the one watt point heat source. The heat flux in the 2D medium is the circumference of the circle encompassing the point source, $C = 2\pi r$. Thus, the heat flux density decreases with the inverse of the circumference. Given the temperature profile in Equation 2.35, the heat flux density is given as the gradient

$$q = -K\nabla T = \frac{1}{2\pi r}. \tag{2.36}$$

Thus, we have a condition for the gradient of our function that

$$\nabla T = -\frac{1}{2\pi K r}. \tag{2.37}$$

The gradient operator ∇ in polar coordinates is given as

$$\nabla T = \frac{\partial T}{\partial r} + \frac{1}{r}\frac{\partial T}{\partial \theta}. \tag{2.38}$$

With our zero order Bessel function K_0 we know that $\frac{\partial K_0}{\partial \theta} = 0$. Thus,

$$\nabla T = \frac{\partial T}{\partial r}. \tag{2.39}$$

Applying the recurrence relation for the modified Bessel equation of the second kind and order zero,

$$\frac{\partial K_0(z)}{\partial r} = -K_1(z). \tag{2.40}$$

Thus,

$$\nabla T = \nabla A_0 K_0(kr) = \frac{\partial A_0 K_0(kr)}{\partial r} = A_0 \frac{\partial K_0(kr)}{\partial r} = -A_0 K_1(kr)k = -A_0(\frac{k}{kr}) = \frac{-A_0}{r}. \tag{2.41}$$

Finally,

$$\nabla T = \frac{-1}{2\pi K r} = \frac{-A_0}{r}. \tag{2.42}$$

Thus,

$$A_0 = \frac{1}{2\pi K}. \tag{2.43}$$

So the total solution is

$$T(r,t) = \frac{1}{2\pi K} K_0(kr) e^{j\omega t}. \tag{2.44}$$

This solution matches that given by Carslaw in *Conduction of Heat in Solids* for a periodic line source in 3D, which by symmetry has the same solution as the 2D polar symmetry

situation. This solution is given for a heat release rate of $Q = \rho c e^{j\omega t}$ as

$$T(r,t) = \frac{1}{2\pi\alpha} e^{j\omega t} K_0(\sqrt{\frac{j\omega}{\alpha}} r). \tag{2.45}$$

Our solution considers a heat release rate of $Q = e^{j\omega t}$, thus for the linear input-output relationship, the solution from Carslaw can be modified with $\alpha\rho c = K$ as

$$T(r,t) = \frac{1}{2\pi K} e^{j\omega t} K_0(\sqrt{\frac{j\omega}{\alpha}} r), \tag{2.46}$$

which is equal to our solution.

2.3.3 3D Green's Function

The solution is similar for 3D, where the Laplacian is expanded in spherical coordinates.

Applying separation of variables to T, we write

$$T(r,\theta,\phi,t) = T(r)T(\theta)T(\phi). \tag{2.47}$$

Expanding the Laplacian and taking all angular derivatives to be zero by symmetry,

$$\frac{\partial T}{\partial t} = \alpha(\frac{\partial^2 T}{\partial r^2} + \frac{2}{r}\frac{\partial T}{\partial r}). \tag{2.48}$$

We can note here that with no angular dependence in either case, the Laplacian in polar and spherical coordinates differs only by a factor of two in the radial first derivative term.

Again taking sinusoidal dependence of the solution,

$$e^{j\omega t}\frac{\partial^2 T(r)}{\partial r^2} + e^{j\omega t}\frac{2}{r}\frac{\partial T(r)}{\partial r} = \frac{j\omega}{\alpha} e^{j\omega t} T(r). \tag{2.49}$$

Finally we have the modified spherical Bessel equation of zero order

$$r^2\frac{\partial^2 T(r)}{\partial r^2} + 2r\frac{\partial T(r)}{\partial r} = r^2\frac{j\omega}{\alpha}T(r). \tag{2.50}$$

The solution can be written with the modified spherical Bessel functions of the second kind and order zero

$$T(r,t) = A_0 k_0(kr)e^{j\omega t}. \tag{2.51}$$

To determine the value of the coefficient A_0, we apply the forcing function of 1 W flux at the origin.

For the radially symmetric function in Equation 2.51, the gradient is just the radial derivative

$$q = -K\nabla T = -K\frac{\partial T}{\partial r}. \tag{2.52}$$

Thus,

$$q = -K\nabla T = -K\frac{\partial}{\partial r}A_0 k_0(kr)e^{j\omega t}. \tag{2.53}$$

Applying the differential relation for $k_0(r)$ that $\frac{\partial}{\partial r}k_0(x) = -k_1(x)$,

$$-K\frac{\partial}{\partial r}A_0 k_0(kr) = kA_0 K k_1(kr)e^{j\omega t}. \tag{2.54}$$

We apply the divergence theorem that the flux density must decrease in proportion to $\frac{1}{4\pi r^2}$ such that the outward flux is constant as the surface area of enclosing surface increases radially

$$q = \frac{1}{4\pi r^2}. \tag{2.55}$$

$$kA_0K\frac{e^{-kr}(kr+1)}{(kr)^2} = \frac{1}{4\pi r^2} \tag{2.56}$$

at $r = 0$.

Finally,

$$A_0 = \frac{k}{4\pi K}. \tag{2.57}$$

Thus, the solution, using the expansion for $k_0(kr)$ is

$$T(r,t) = \frac{k}{4\pi K}\frac{e^{-kr}}{kr}e^{j\omega t}. \tag{2.58}$$

Simplifying the above and using $k = (1+j)\beta$,

$$T(r,t) = \frac{1}{4\pi Kr}e^{-\beta r}e^{j(\omega t-\beta r)}. \tag{2.59}$$

2.3.4 Spatial Frequency Domain Solution

The SMI system maps a three-dimensional region of refractive index to a two-dimensional image of optical pathlength. The precise formulation of this mapping requires a knowledge of the phase accumulation effect of the Gaussian imaging beam as well as its scattering from the sample. To avoid this formulation, the highly confocal nature of SMI due to the singlemode fiber-coupling in the system can be applied. Thus, we assume that the temporally-modulated optical pathlength change produced by the photothermal signal is sampled by SMI only at a single plane corresponding to the focal plane of the imaging beam. The 3D distribution of temperature produced by the thermal point source can be simplified as a horizontal plane passing through the origin in Equation 2.59.

Through the linearity of the thermal wave equation in Equation 2.16, the spatial frequency

response of the thermal wave can be described with a two-dimensional Fourier transform. As described, we assume the SMI system samples the 3D point-spread function at the $z = 0$ plane of Equation 2.59, where $r = \sqrt{x^2 + y^2 + z^2}$. Thus, we apply the Fourier transform to the now 2D function in Equation 2.59 with $r = \sqrt{x^2 + y^2}$. As the point spread function has radial symmetry, the 2D Fourier transform can be described as a Hankel transform as

$$H(k) = 2\pi \int_0^\infty J_0(kr) r h(r) dr, \tag{2.60}$$

where $k = \sqrt{k_x^2 + k_y^2}$ and $h(r) = \frac{1}{4\pi K r} e^{-\beta r} e^{j(\omega t + \beta r)}$ with $r = \sqrt{x^2 + y^2}$.

Thus, the spatial frequency response is

$$H(k) = \frac{e^{j\omega t}}{2K\sqrt{k^2 + 2j\beta^2}}. \tag{2.61}$$

A radial cross-section of the amplitude of the spatial transfer function in Equation 2.61 for multiple β is given in Figure 2.1

One chief point visible from both Equation 2.61 and Figure 2.1 is that at any spatial frequency k, the amplitude response of the PT imaging method is greater for a smaller thermal wavenumber β. Thus, for any spatial frequency of interest, a lower modulation frequency and thus lower thermal wavenumber will produce a higher measured signal energy. This point is of interest when selecting the modulation frequency used to generate the PT signal. It is commonly perceived in the photothermal literature that a high modulation frequency is necessary to produce high spatial resolution PT images. This point is true for the case of thermal lens detection of the PT signal, where a large gradient in temperature is necessary to produce a thermal lens. However, as seen in Figure 2.1, the signal energy in high spatial frequencies, and thus the energy of interest for high resolution images, is actually higher at

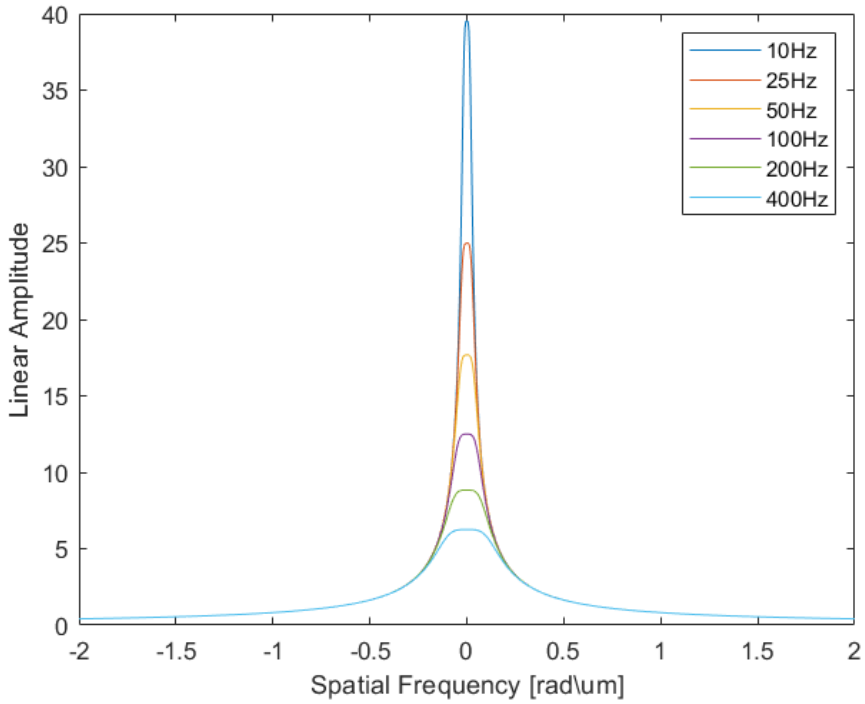

Fig. 2.1. Photothermal imaging spatial frequency response, multiple modulation frequencies shown.

lower modulation frequencies. With examination in only the original image domain, these high resolution features can be obfuscated by larger energy lower spatial frequencies at low modulation frequencies, but the information is not lost. Thus, the PT imaging theory could be used to deconvolve the measured PT image to reduce the amplitude of the lower spatial frequencies rather than increasing the modulation frequency experimentally, which may not be possible due to apparatus limitations.

2.4 Numerical Simulation

To verify the Green's functions solutions in multiple dimensions, the heat equation in each dimension was discretized and solved numerically with a finite difference method.

2.4.1 1D

As derived as Equation 2.18 in the previous section, the *sourced* one-dimensional Heat diffusion equation is

$$\alpha \frac{\partial^2 T}{\partial x^2} + \frac{P}{\rho c} = \frac{\partial T}{\partial t}. \tag{2.62}$$

To modify this equation into a form we can solve numerically, we discretize the temporal and spatial derivatives. We will discretize the derivatives using the Backward-Time, Central Space (BTCS) stencil, which is the implicit method for solving the finite difference equations [26]. The discretization is then given as

$$\frac{T_j^n - T_j^{n-1}}{\partial t} = \alpha \frac{(T_{j+1}^n - 2T_j^n + T_{j-1}^n)}{(\partial x)^2} + \frac{\alpha}{K} P. \tag{2.63}$$

We simulate the free-space solution with perfectly damped boundary conditions. In other words, we simulate a finite region with the temperature at the boundary of this region as zero. If the diffusion equation was instead the undamped wave equation, this method of simulation would pose a problem, as we would generate a standing-wave solution due to the conditions on the boundary. However, we will use the knowledge of the theoretical solution of the diffusion equation that the wave is spatially damped, and decays exponentially with distance from the source. Thus, with the simulation region large enough that the wave is largely decayed before it reaches the boundary, the zero-temperature boundary condition will be adequate to simulate the correct temperature field within the boundaries.

In the one-dimensional case, the boundary condition is then

$$T_0^n = 0 \tag{2.64a}$$

and

$$T_J^n = 0. \tag{2.64b}$$

In other words, for all time points, we take the left and right boundary values to be zero.

We also take the initial condition that

$$T_j^0 = 0, \tag{2.65}$$

or that for all spatial points, the initial temperature is zero.

We also have the knowledge of our source P_j^n at all time points n and spatial locations j, along with our knowledge of the medium parameters α, ρ, and c. To simulate the heat diffusion to a temporally harmonic point source, we take

$$P_j^n = \begin{cases} e^{j\omega t(n)} & j = \frac{J}{2} \\ 0 & j \neq \frac{J}{2}. \end{cases} \tag{2.66}$$

Thus, considering again Equation 2.63 with the conditions in Equation 2.64 and Equation 2.65, we consider the first unknown time point, $n = 1$.

Examining Equation 2.63 for $n = 1$, we can see that T_j^n is the point of interest, T_j^{n-1} is zero for $n-1 = 0$, and T_{j-1}^n and T_{j+1}^n are the temperatures of the adjacent points at the same time point. If the simulation region consisted only of three spatial points, i.e. $j = 0, 1, 2$, these adjacent points would be the boundaries, and their values would be known for all n. For

$J > 3$, these points are also unknown, and we write a new equation at each adjacent point at time point n until we reach the boundaries. These equations can be solved simultaneously to fully determine the temperatures at each point for each time n. Thus, the *implicit* method is described, as the temperature of interest T_j^n is described implicitly and must be solved as a system with the other points.

Figure 2.2(a) shows the temporal evolution of the temperature in the spatial and temporal evolution, while (b) shows the phase relationship of the temperature at the source point and 10 µm and 20 µm away.

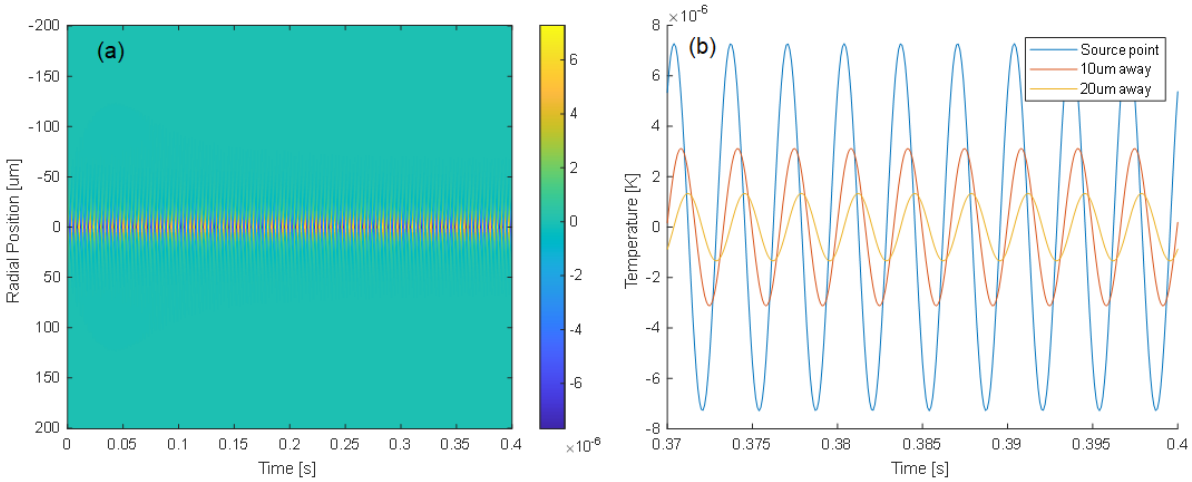

Fig. 2.2. 300 Hz 1D solution: Temporal temperature evolution [K] (a), temporal trace (b).

Figure 2.3 shows the photothermal amplitude and phase at each spatial position in the one-dimensional simulation. A near perfect match is visible in the amplitude curves, while a deviation between simulation and theory is visible in the phase curves after 50 µm away from the source. At these positions, there is some propagation of numerical errors resulting from the sensitivity of the extracted phase to the simulation SNR. In other words, for positions above 50 µm away from the source point, the phase extracted from the analytic signal is an equal contribution of both the numerical signal as well as numerical noise from the floating point quantization. After 100 µm away from the source, the signal is largely zero from the

initial conditions of the simulation, so the phase is flat

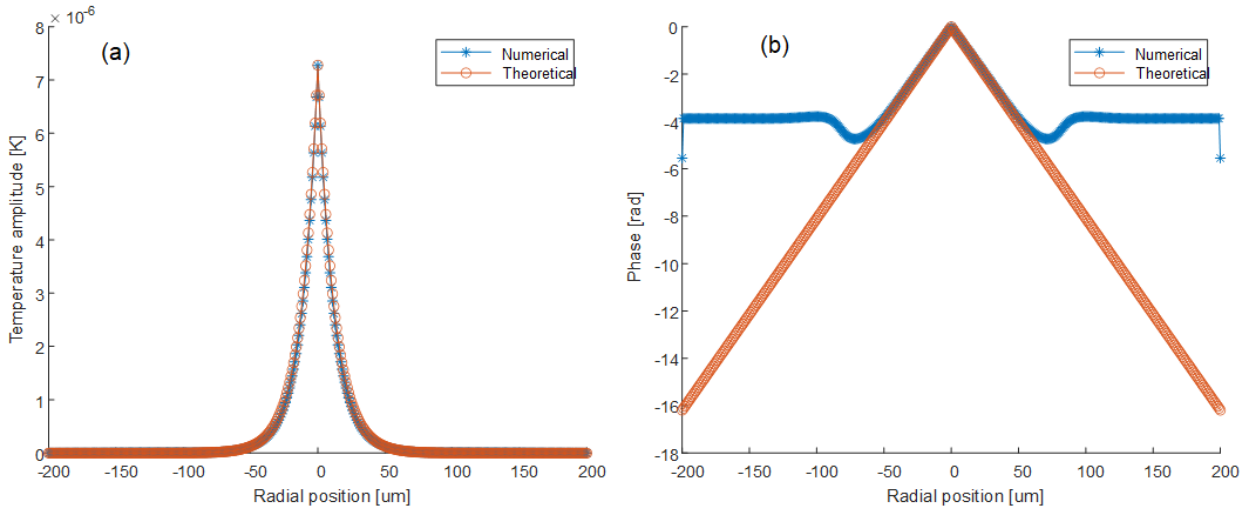

Fig. 2.3. 300 Hz 1D solution: photothermal amplitude (a), photothermal phase (b).

2.4.2 2D

The two-dimensional Green's function was simulated identically to the one-dimensional case. The implicit finite-difference method was used to solve a set of simultaneous equations for each time point. A modulated thermal point source was placed in the center of the field, and the amplitude and phase curves were plotted through a radial cross-section. Figure 2.4 shows the simluated and theoretical radial cross-sections of the photothermal amplitude and phase. The amplitude has a near perfect match between theory and simulation, while the phase curves experience a similar deviation as in the 1D case.

2.4.3 3D

For the three-dimensional case, the explicit, or forward time centered-space (FTCS) stencil, method was used. This method requires only calculating the future value of each point based

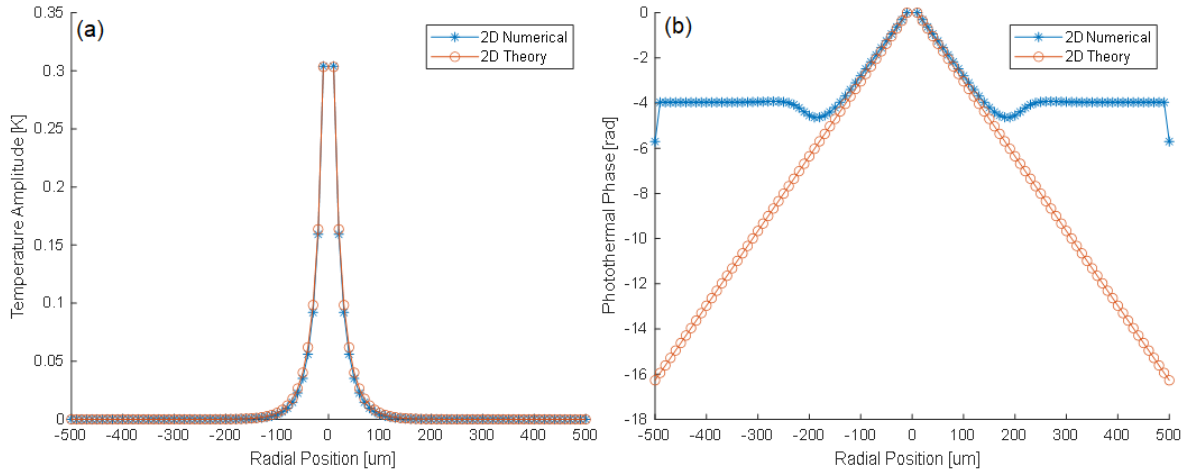

Fig. 2.4. 50 Hz 2D solution: photothermal amplitude (a), photothermal phase (b).

on its previous value and adjacent points, and thus is less memory intensive for the higher dimensional case. This method has the restriction of a particular relationship between the temporal and spatial spacing for a numerically stable solution, but this constraint can be accommodated.

Water medium

The Green's function for the full space of water was calculated identically as the other dimensions, with a periodic thermal source placed in the center of the simulation space. The amplitude and phase were extracted after the region had come to a steady sinusoidal state. Figure 2.5 shows the amplitude and phase radial cross-sections through the source point. The singularity of the temperature at the source point is removed from the plot for both the numerical and theoretical solution.

Glass-water interface

For the case of interest in this experimental setup the thermal medium consists of a half-space of water atop a half-space of glass that is the substrate for the sample mirror. To determine

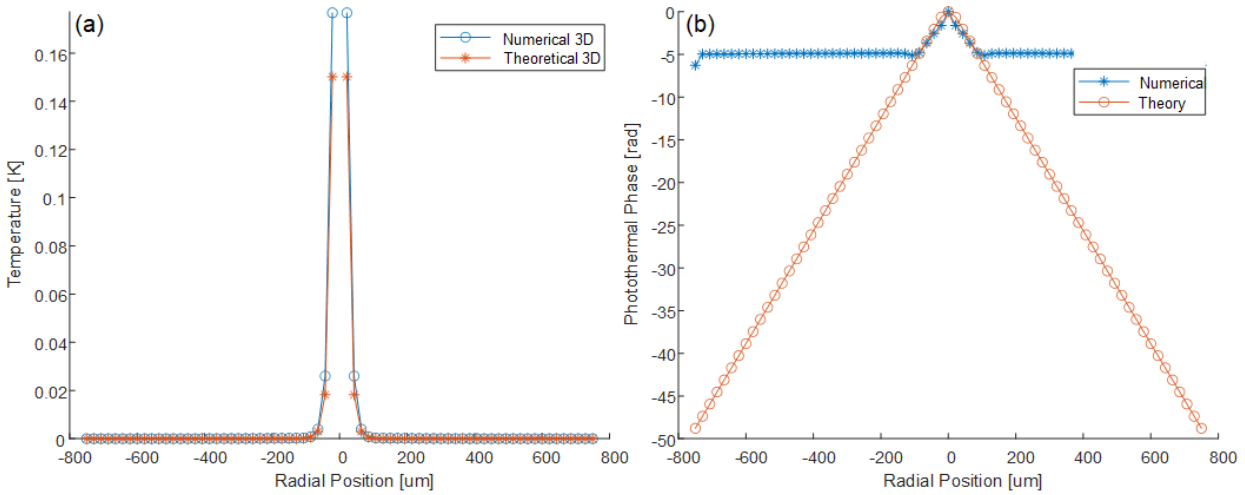

Fig. 2.5. 200 Hz 3D solution water: photothermal amplitude (a), photothermal phase (b).

the effect of this medium compared to the full space of water, the numerical simulation was performed in 3D with a point heat source positioned in the water half-space atop the glass interface.

Figure 2.6 plots the amplitude and phase radial cross-sections of the numerical simulation of the glass-water medium through the source in the water and compares to the theoretical curves in Equation 2.59 for a medium consisting of only water. This result gives convincing indication that the glass-water thermal medium is a sufficient candidate for the verification of the thermal point spread function theory for the full space of water, with some caution in quantitative matching. In other words, the temperature distribution surrounding a point thermal source near the interface of glass and water is qualitatively similar to the temperature distribution surrounding a point thermal source in a homogeneous medium of water.

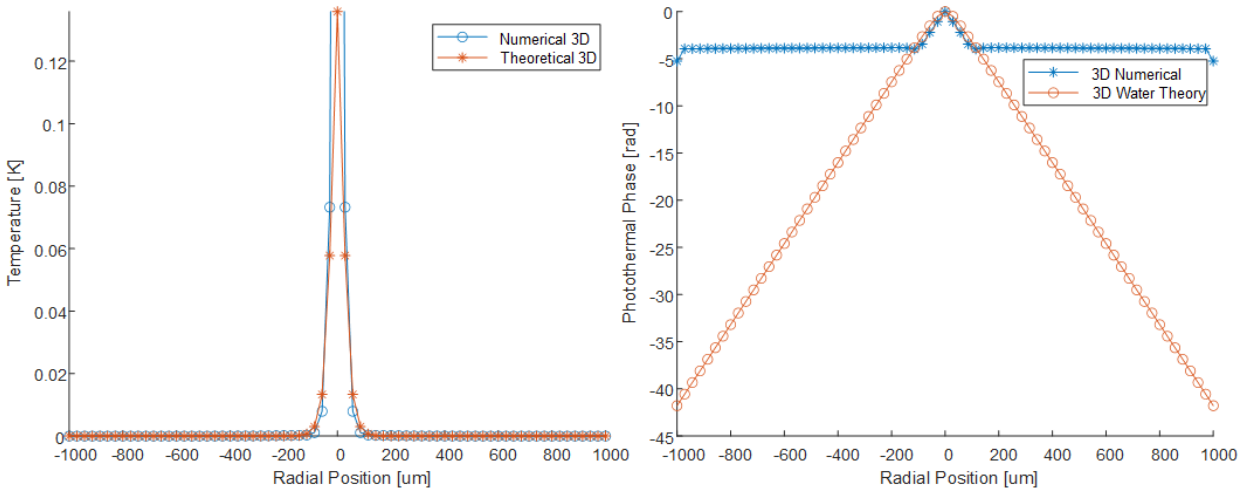

Fig. 2.6. 200 Hz 3D solution water-glass: photothermal amplitude (a), photothermal phase (b).

Chapter 3

Methods

3.1 Aliased-signal Detection Scheme

With the imaging rate flexibility of the SMI system, the generated photothermal signal can be undersampled or oversampled. Fixing the galvonometric mirror, a single line is imaged at the 78 kHz sampling rate of the spectrometer. Alternatively, scanning the galvonometric mirror builds up two-dimensional images with a reduced imaging rate, for example 66 Hz or 131 Hz depending on the scanning resolution.

To verify the equivalency of the photothermal amplitude signal when undersampled and oversampled, a 1 kHz and 3 kHz signal was measured in the stationary SMI configuration and the 2D imaging configuration. In the stationary configuration, the 1 kHz signal is heavily oversampled by the spectrometer's imaging rate of 78 kHz, and a single 1024 pixel line of optical pathlength changes is measured. In the scanning configuration, the 1 kHz signal is undersampled by the 66 Hz imaging rate for 1024 by 1024 pixel images. Figure 3.1 shows the temporal amplitude spectral density from the SMI system under 1 kHz photothermal pumping for stationary line acquisition (a) and full-field imaging (b). The extracted photothermal amplitude radial profiles are visible in Figure 3.2 at the fundamental frequency of 1 kHz (a) and its first odd harmonic of 3 kHz (b). It can be seen in Figure 3.2 that the acquired profile of the PT signal is the same for both oversampled and undersampled cases. Noise energy aliasing into the shorter Nyquist band in the full-field imaging case produces a higher noise

background than in stationary acquisition.

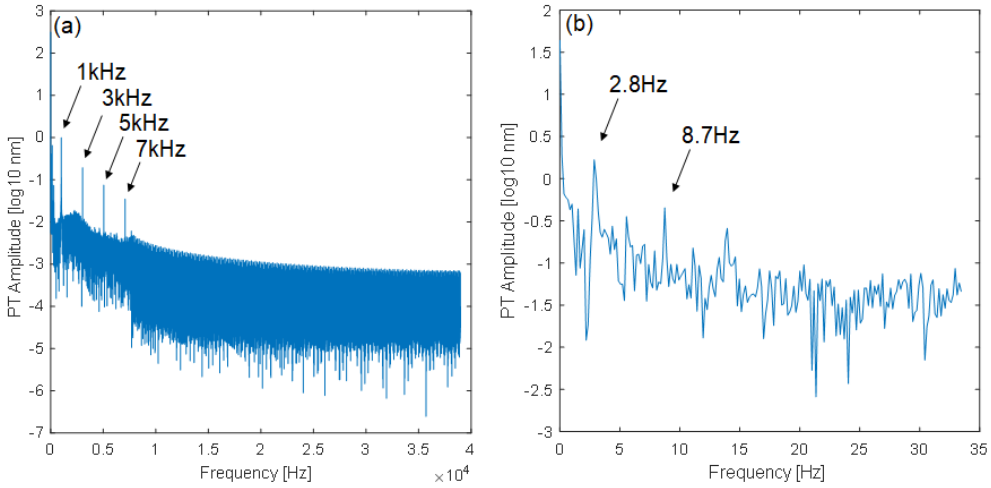

Fig. 3.1. OPL Temporal Amplitude Spectrum with 78 kHz sampling (a) and 66 Hz sampling (b).

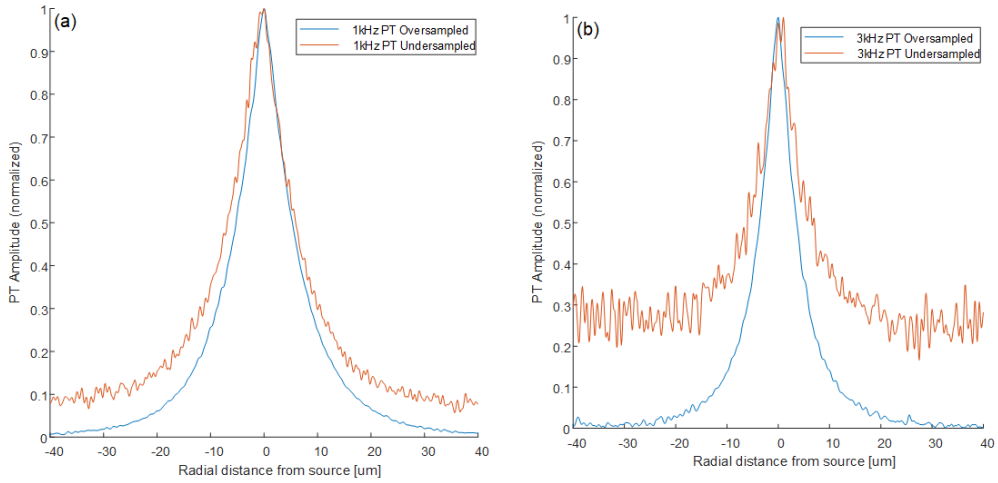

Fig. 3.2. Oversampled and undersampled PT signal at 1 kHz (a) and 3 kHz harmonic (b).

To demonstrate the high modulation frequency resolving ability of the photothermal signal by the SMI system, a 10 kHz signal is induced and imaged in a full-field configuration with an image resolution of 1024 spectral pixels by 512 scanning pixels. With the minimum required galvo flyback time per scan, the 2D imaging rate is 131 Hz. Figure 3.3 shows the location of the aliased signal with 131 Hz sampling and a radial cross-section of its amplitude profile.

At a sampling rate of precisely 131.206 Hz, the 10.5552 kHz signal has a calculated alias frequency of 58.72 Hz after sampling. The experimentally determined alias signal appears at 58.8 Hz in good agreement with the calculated position. With the 100 µs period of the 10 kHz signal, the typical 12 µs exposure time of the SMI system is short enough to avoid signal averaging effects. By lowering the SMI exposure time, higher modulation frequencies above 10 kHz could be measured.

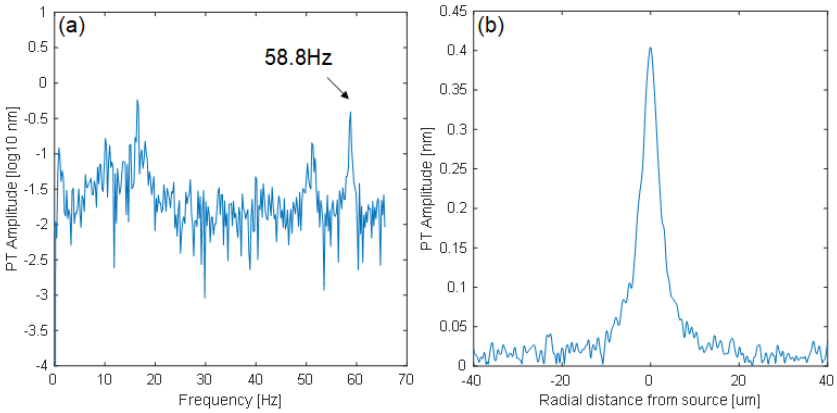

Fig. 3.3. 10 kHz PT Signal: Aliased signal detection (a) and radial amplitude cross-section (b).

3.2 Photothermal Point-source

To generate a photothermal point source, the inherent absorption of 532 nm light by chromium was used. The USAF 1951 resolution target, containing a 150 nm thick layer of chromium sputtered onto a polished glass substrate, served as a target for the absorption of focused green light. A 50 µL drop of water was placed on the chromium, followed by a number one coverslip shouldered by two 50 µm thick pieces of double-sided tape. The green laser was collimated into the back aperture of the microscope objective to be focused on the chromium layer in the same manner as the imaging beam. With the diffraction-limited performance of the microscope objective at a numerical aperture of 0.65, the beam-waist of the focused

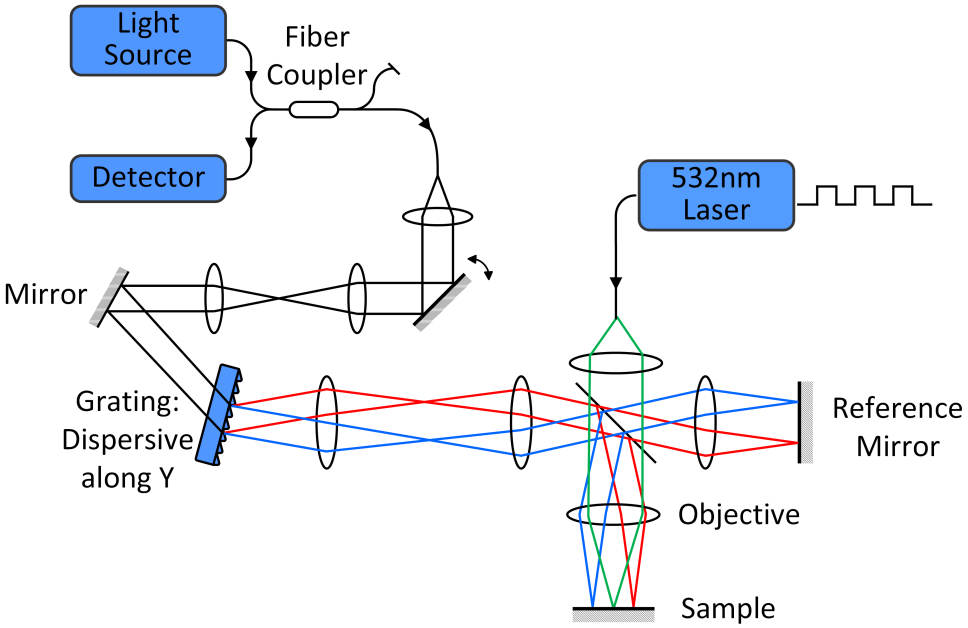

Fig. 3.4. Spectral Modulation Interferometry, PT Point Source.

green laser was confidently less than one micron. Thus, although not a true point source with infinitesimal extent, the photothermal source was much smaller than the theoretical thermal wavelength and amplitude profile. Figure 3.4 shows the optical system diagram for the photothermal point source experiments. The SMI system is largely unchanged from its usual microscopy configuration, with the addition of the collimated green laser incident upon the interferometer beamsplitter.

One inconvenience related to the coupling of the green pumping laser into the interferometer is the mismatch between pump and probe wavelengths. The probe interferometer of the SMI system operates in the near-infrared region; thus, of all the imaging optics are coated to eliminate near-infrared reflections. The visible light pump laser therefore has reflections off of the interferometer beamsplitter, and the high power pump generates multiple reflections from the beamsplitter interfaces, not just the first interface. Therefore, alignment of the pump laser in the sample plane of the SMI system is difficult, as a camera sensor conjugated

to this plane is filled with the reflection of the collimated pump beam. Thus, the most convenient way to align the green pump in the sample plane is to generate a photothermal signal itself, and look at the location of the maximum point of the PT image.

Another consideration in this optical alignment is the dispersion of the microscope objective. To best approximate a thermal point source, the green pump beam must be best focused on the surface of the chromium mirror. Also, for best operation of the SMI system, the near-infrared imaging beam must also be focused on the surface of the chromium. Thus, the 532 nm pump and the near-infrared imaging beam with wavelengths from 810 nm to 870 nm must be focused simultaneously by the objectives. To verify this simultaneous focusing was present, the imaging beam was focused as normally done in SMI by maximizing the brightfield intensity on the spectrometer. In this position of best focus, the reflected portion of the pump beam was coupled out of the system onto a power meter. The sample stage was adjusted vertically, and it was verified that the pump beam reflection was maximized at the same vertical position of the mirror as the imaging beam.

3.3 Wide-field Photothermal Imaging

For the wide-field photothermal imaging of cellular samples, the pumping source should be made as large as possible to pump the entire sample simultaneously, ideally with uniform intensity spatially. To configure the pumping source in this manner, a 4f system was established between the mode field of the singlemode fiber and a plane of incidence oblique to the sample. In the plane normal to the propagation of the Gaussian laser beam, the focused beam diameter was 45 µm. In the sample plane, the beam is obliquely projected onto the mirror based on the angle of incidence. In this plane, the oblique profile of the laser has a beam diameter of 135 µm. Thus, the pumping laser covers a significant portion

of the 100 µm by 100 µm SMI field-of-view. This configuration has an advantage beyond the necessity of increasing the size of the pumping beam. As the photothermal pumping source is completely independent of the microscope optics, the wavelength of the pump source need not be compatible with the near-IR optics used in the SMI system. Figure 3.5 shows the optical system diagram of the SMI system set up for photothermal imaging cellular samples. The oblique and independent illumination of the sample plane by the photothermal pumping source is visible.

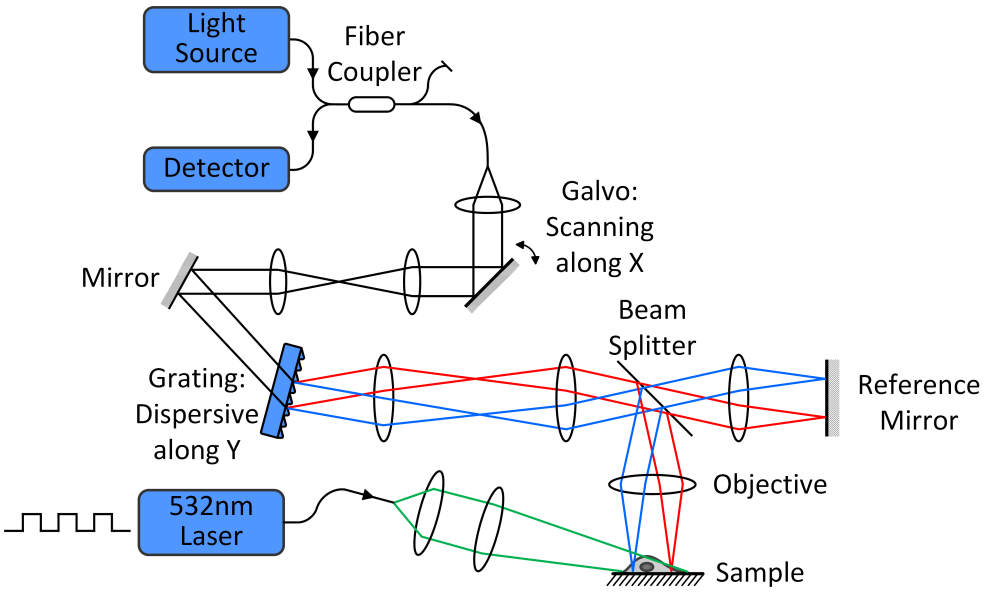

Fig. 3.5. Spectral Modulation Interferometry, Wide-field PT Imaging.

To verify the alignment of the pumping source in the sample plane, a dense sample of 25 µm diameter glass beads was prepared and placed in the sample plane. The beads were dispersed in distilled water via sonication, and a drop of the bead suspension was placed on the mirror with a number one coverslip atop it.

A CMOS camera was aligned into the SMI system such that its sensor plane was conjugate to the sample plane. The glass beads were illuminated with the photothermal pumping source, and the image of the scattered green light was recorded with the camera. A Gaussian fit was

performed in the oblique and non-oblique dimensions of the image of the beam to determine the approximate beam diameters, as shown in Figure 3.6. As the pump beam was aligned without propagation through the imaging optics, there were no spurious reflections of the visible pump beam by the near-infrared coated optics. Thus, the method of conjugating a CMOS sensor to the sample plane worked without the issues preventing this arrangement for the point source pump alignment.

Some care must be taken in this oblique alignment of the visible pump beam. The most basic precaution is that the high optical power pump beam is coupled into the system without the use of an optical cage system. The optical alignment being completely freehand, the reflection of the high power laser off of the mirror must be blocked with a screen to avoid dangerous propagation of the beam into the laboratory area. The freehand nature of the pump alignment in this configuration also requires careful adjustment of the fiber and 4f system to ensure the focused beam is within the 100 µm by 100 µm SMI field-of-view, which can be assured by the CMOS camera. A final consideration directly related to the oblique incidence of the pump beam onto the sample plane is the possible clipping of the beam by the sample objective. The incidence angle to the normal vector of the mirror plane must be large enough, i.e. oblique enough, that the front lens assembly housing of the sample objective does not intersect the beam. However, with too oblique an angle, the power density will be reduced as the projection of the beam onto the sample plane will be increased in area. Thus, for this alignment, the projected beam size visible with the CMOS sensor was reduced to the greatest extent possible without clipping the beam.

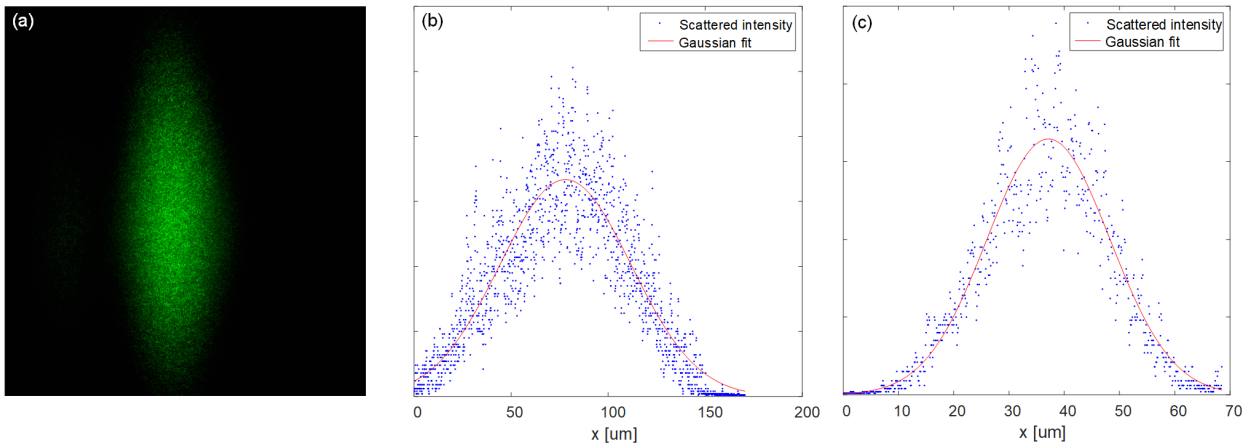

Fig. 3.6. Wide-field PT imaging: pumping source profile (a), oblique incidence cross-section (b), non-oblique cross-section (c).

Chapter 4

Results

4.1 Photothermal Point Source

To measure the point spread function of the photothermal imaging system, the 532nm green pumping laser was collimated into the back aperture of the microscope objective, so the beam was focused onto the chromium resolution target. The absorption of green light by the chromium layer created the photothermal source of size smaller than the thermal diffusion length.

The amplitude and phase of the photothermal signal were extracted for a 5 Hz source. A vertical cross-section was selected to extract the radially symmetric amplitude and phase. In the SMI system, vertical lines are imaged simultaneously, so no correction factor is necessary to observe the photothermal phase along this line. It can be easily seen in Figure 4.1 that the photothermal phase varies linearly with radial position, as predicted by the theory of an outgoing thermal wave.

To determine the effect of the chromium layer on the photothermal signal compared to the glass-water interface, the photothermal pumping source was positioned near the edge of the chromium layer and its radial cross-section was examined. Figure 4.2(a) shows the wrapped optical pathlength image of the chromium edge sputtered on the glass substrate immersed in water. Figure 4.2(b) shows the photothermal amplitude image for the thermal source

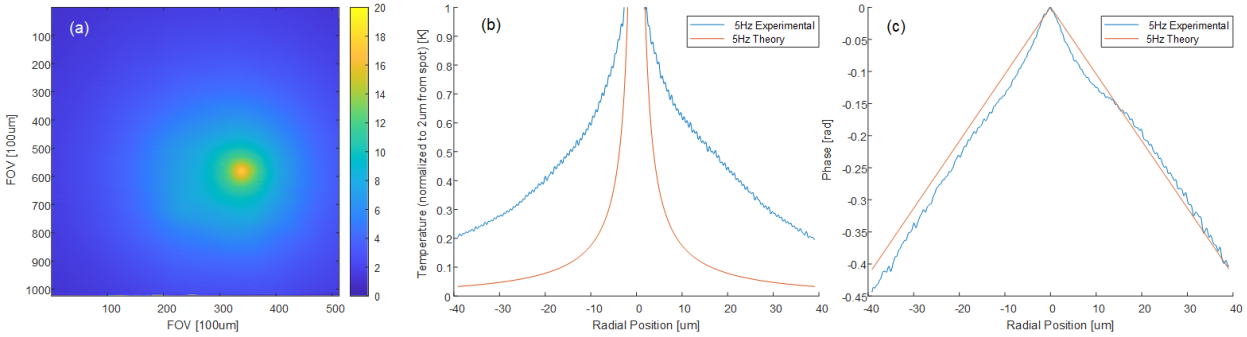

Fig. 4.1. 5 Hz Photothermal point source: Amplitude image (a), amplitude radial cross-section (b), phase radial cross-section (c).

positioned close to the edge of the chromium layer.

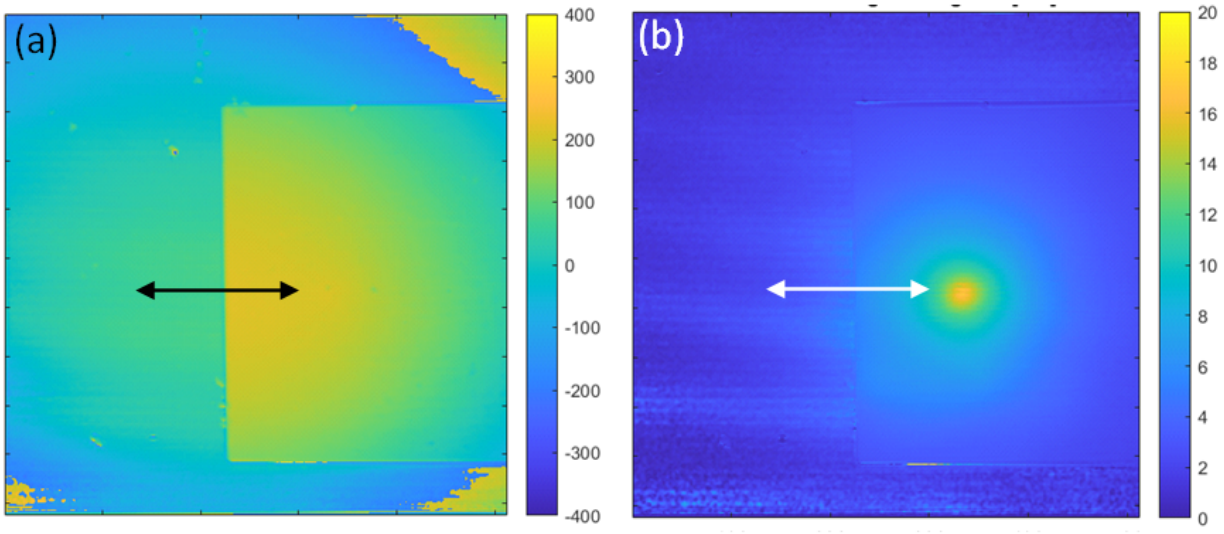

Fig. 4.2. Imaging the edge of the chromium resolution target. Optical pathlength [nm] (a), photothermal amplitude [nm] (b).

A horizontal cross-section through the photothermal signal is then compared to the same cross-section in optical pathlength in Figure 4.3. In the PT signal cross-section, it can be seen that at the edge of the chromium layer, the PT signal is unperturbed by the transition from the chromium-water interface to the glass-water interface. Thus, it can be concluded that the chromium layer has minimal effect on the propagation of the photothermal wave

in the water medium. The lower SNR of the PT signal in the glass region compared to the chromium region due to the reduced optical reflection at the water-glass interface compared to the water-chromium interface is also visible.

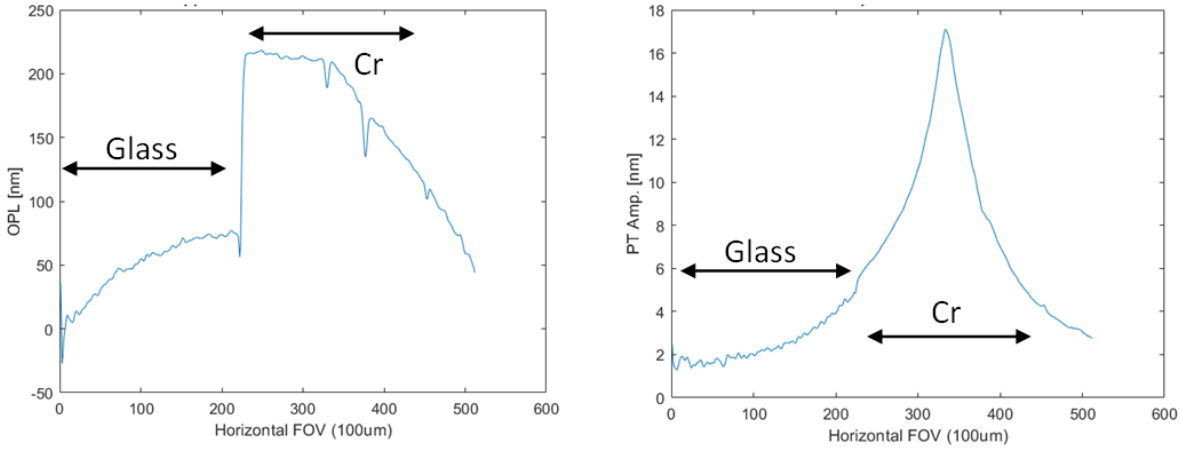

Fig. 4.3. Chromium edge horizontal cross-sections in optical pathlength (a), photothermal amplitude (b).

The relationship between photothermal amplitude and pumping power was also established. Based on the linear partial differential equation that governs the diffusion of heat, the relationship between thermal source power and the temperature distribution generated by the source should also be linear. Figure 4.4(a) shows such a linear relationship. The peak of the photothermal amplitude response measured as an OPL amplitude in nanometers is extracted and plotted against various optical powers, taken as the amplitude coefficient of the fundamental frequency of the pumping waveform in milliwatts. The conversion of this optical power to thermal power is roughly 45%, or the power transmission coefficient for 532 nm light incident into chromium which is entirely absorbed.

At 2.5mW optical power, multiple modulation frequencies were used and their amplitude and phase responses were extracted. Figure 4.5 shows the amplitude response at these frequencies.

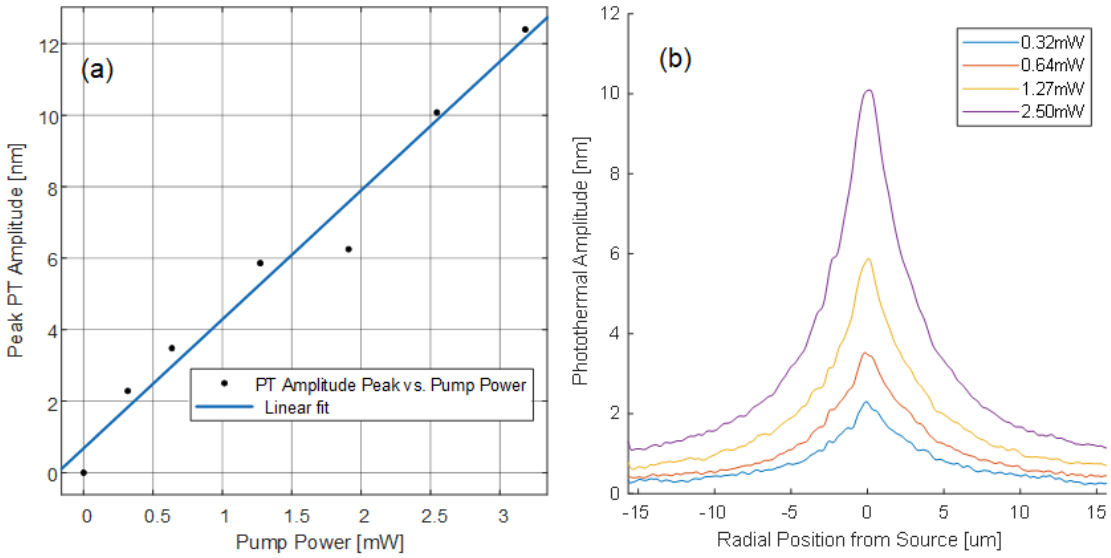

Fig. 4.4. Photothermal power response, measured at 10 Hz: PT amplitude vs laser power (a), radial profiles of selected source powers (b).

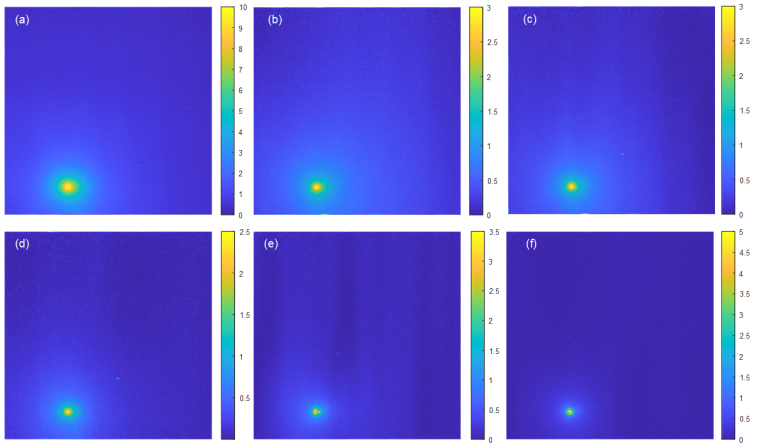

Fig. 4.5. PT Modulation frequency Response amplitude images with 2.5 mW pump power, FOV 100 µm x 100 µm: 10 Hz (a), 25 Hz (b), 50 Hz (c), 100 Hz (d), 200 Hz (e), 400 Hz (f).

The photothermal phase was also extracted from the measured photothermal signal from a region surrounding the photothermal source for which there was adequate SNR. Figure 4.6 shows the radial phase profile in a linear phase region around the source point for each frequency. A linear fitting was performed to estimate the photothermal wavenumber (slope) for each modulation frequency.

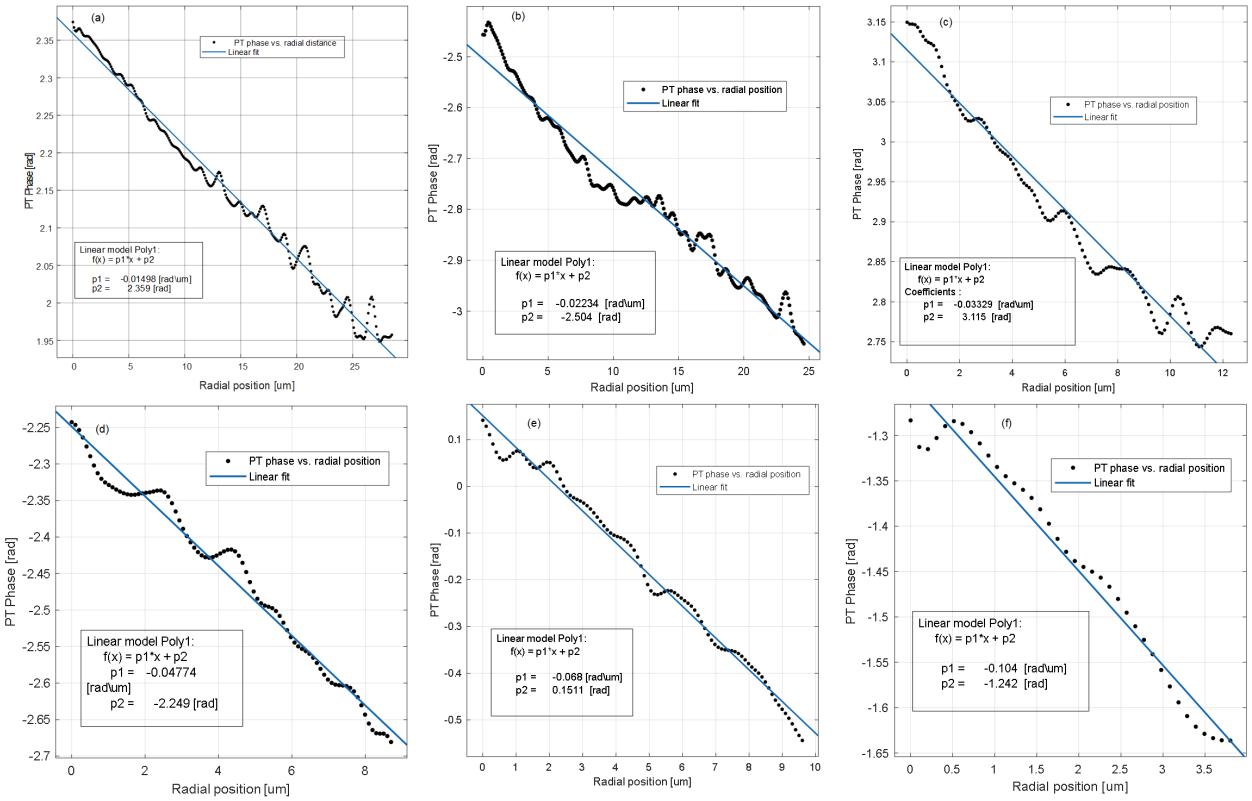

Fig. 4.6. PT frequency response phase profiles with 2.5 mW pump power, FOV 100 µm x 100 µm: 10 Hz (a), 25 Hz (b), 50 Hz (c), 100 Hz (d), 200 Hz (e), 400 Hz (f).

The diffusion equation is naturally dispersive, as the spatial and temporal frequency relationship is not linear. The thermal wavenumber is given as the real part of Equation 2.17, or

$$\beta_{Re} = \sqrt{\frac{\omega}{2\alpha}}. \tag{4.1}$$

Thus, the wave speed given as $\frac{\omega}{\beta}$ is

$$v_p = \frac{\omega}{\beta} = \frac{\omega}{\sqrt{\frac{\omega}{2\alpha}}} = \sqrt{2\alpha\omega}. \tag{4.2}$$

The dispersion relation of the thermal wave in a water medium can then be determined using the fitted wavenumbers of Figure 4.6 and the corresponding modulation frequencies. Figure

4.7 shows the experimental thermal dispersion relation for water simultaneously with the theoretical dispersion relation.

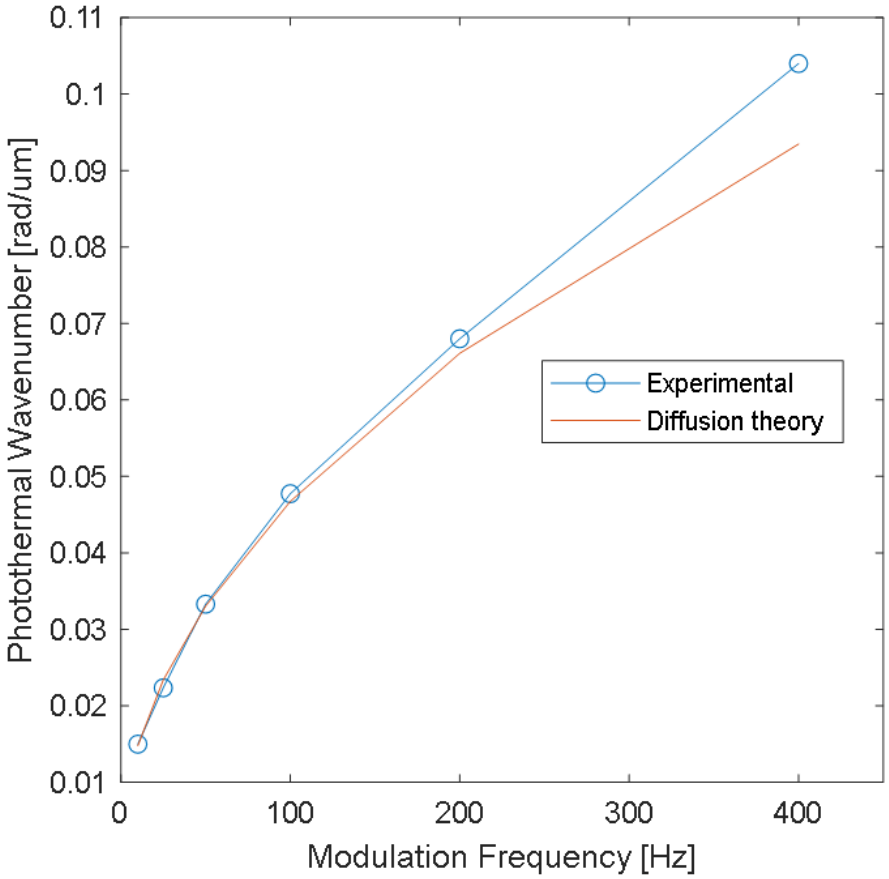

Fig. 4.7. Photothermal dispersion relation, β vs. $\frac{\omega}{2\pi}$.

4.2 Red Blood Cells

The wide-field photothermal imaging of human red blood cells was also performed. Figure 4.8(a) shows an average OPL image of the red blood cells, while (b) shows the extracted photothermal image at 100 Hz with 532 nm pumping light in the profile shown in Figure 3.6. Figure 4.8(c) and (d) show the temporal and frequency spectrum of the optical pathlength

at various image points. The 100 Hz photothermal signal aliases down to 20 Hz with the 120 Hz SMI sampling.

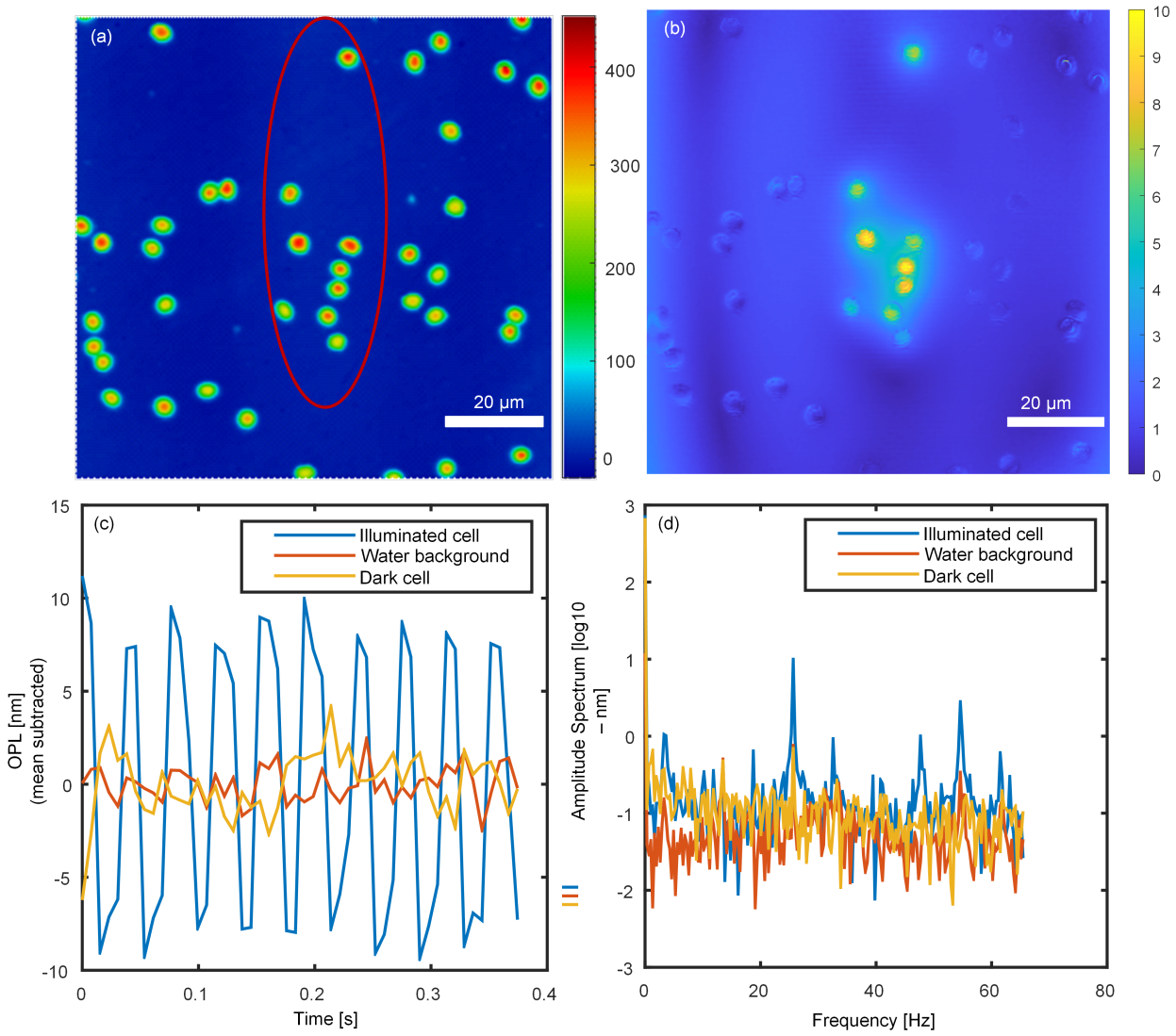

Fig. 4.8. Spectral Modulation Interferometry, wide-field PT imaging: average OPL image (a), 100 Hz PT amplitude image (b), OPL temporal trace (c), OPL temporal amplitude spectrum (d).

To qualitatively examine the measured photothermal amplitude image for the red blood cell sample, the photothermal transfer function was used. Figure 4.9(a) shows a single OPL image of the RBC sample. This image was masked with the Gaussian illumination pattern

with position and beam waists corresponding to the position of the actual pumping beam. The spatial amplitude spectrum was generated for the masked OPL image using a 2D Fast Fourier Transform (FFT), and the theoretical spatial frequency response of the PT imaging system was generated for the 100 Hz pumping modulation. The amplitude spectrum of the RBC OPL image and the PT frequency response were multiplied, and an inverse 2D FFT was applied to generate the simulated PT image for the RBC sample in Figure 4.9(e). Comparing this image to the one measured experimentally in Figure 4.8(b) shows semi-qualitative agreement in the photothermal signal. Especially evident is the photothermal blurring due to the finite width of the PT point spread function. The forward application of the PT frequency response to produce a simulated PT image suggest a strong possibility of removing this diffusive PT tail using a division in the frequency domain by the measured or theoretical PT frequency response to generate optical resolution photothermal images. Important to note is that the resolution of the measured PT images is completely independent of the wavelength of pumping modulation. This resolution is only dependent on the thermal parameters of the sample medium and the modulation frequency of the pumping source. Thus, a sample could be pumped with a particularly long wavelength source, such as mid-infrared radiation or even microwave radiation, and the PT images would have resolution as in Figure 4.8(b). Single micron-scale resolution absorption contrast images could be generated with pump wavelengths in the tens or hundreds of microns.

4.3 Chemically Specific Imaging

To show the chemical specificity of the photothermal imaging technique, a sample with two types of cells was imaged. The human red blood cells, as shown above, absorb 532 nm light due to their high concentration of hemoglobin. The human cheek cells, which contain no

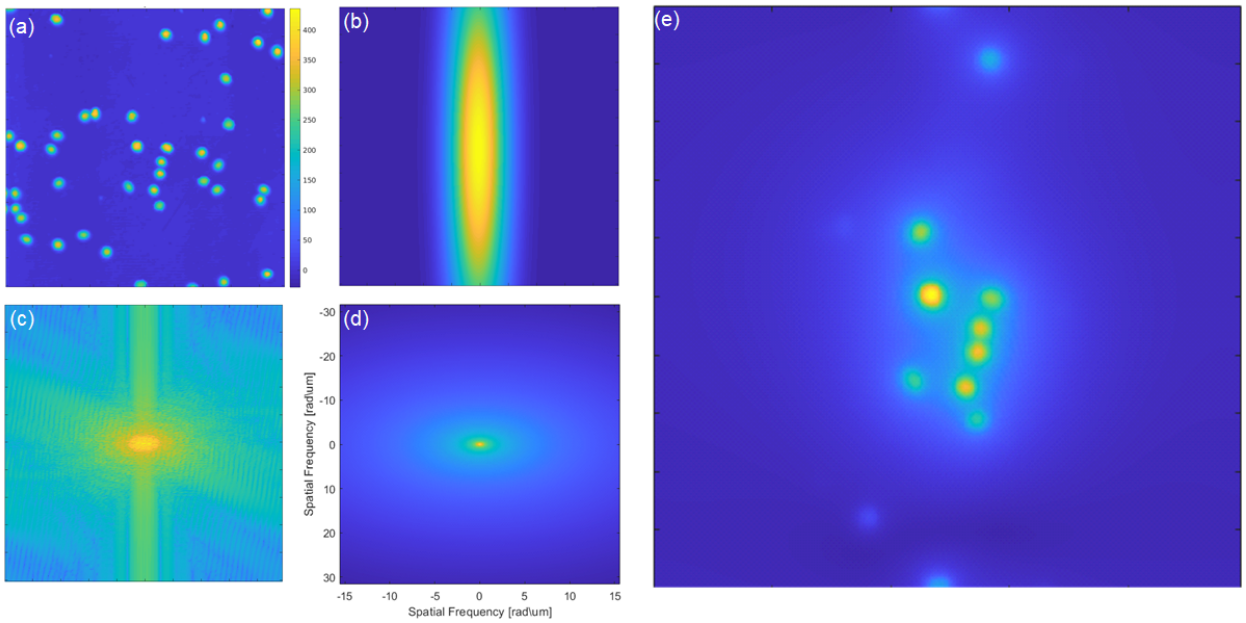

Fig. 4.9. Photothermal image prediction: first frame OPL [nm] (a), pumping mask (b), spatial amplitude spectrum (c), PT spatial transfer function (d), simulated RBC PT image (e).

hemoglobin, absorb little green light and thus do not generate a significant photothermal response to the widefield laser pumping. Figure 4.10 shows the PT imaging method with an absorbing and non-absorbing sample. A phantom signal is visible at the edges of red blood cells not illuminated by the pumping beam. As the photothermal amplitude signal is generated by taking the amplitude of the OPL change at the modulation frequency, any temporal change in the OPL at an image point with energy at the modulation frequency will appear as a photothermal signal. In this case, the vibration of the red blood cells immersed in the liquid medium produces such a signal. The cheek cell, which strongly adheres to the mirror surface, shows minimal lateral movement and thus disappears in the photothermal image with no absorption at 532 nm.

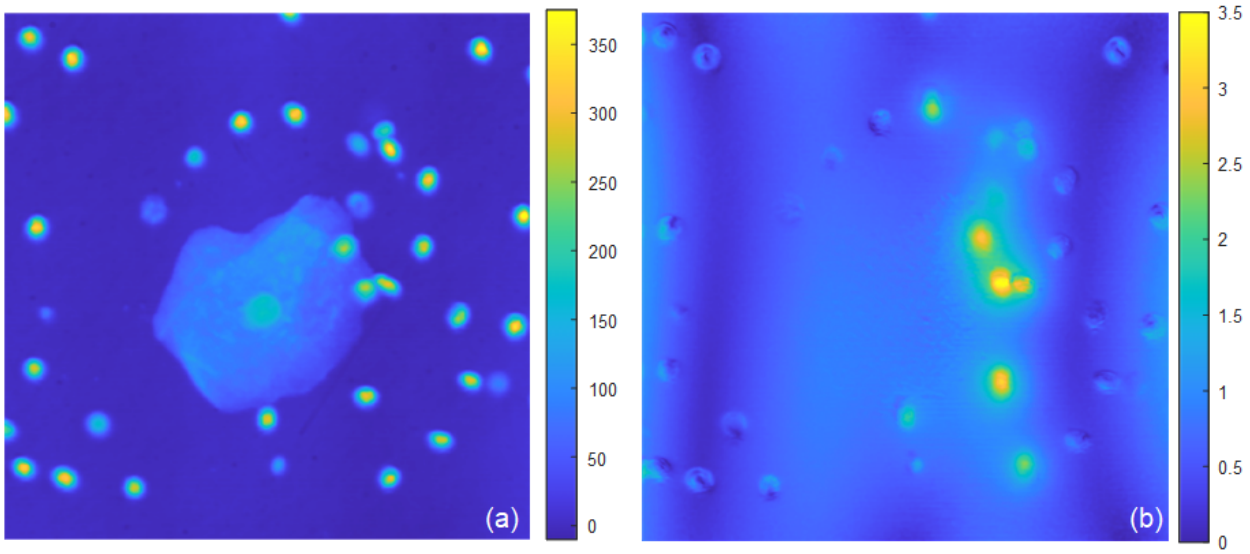

Fig. 4.10. Chemically specific PT imaging: average OPL image [nm] (a), 100 Hz PT amplitude image [nm] (b).

Chapter 5

Summary

This work develops the motivation for using the photothermal effect to generate absorption contrast in cellular samples that can be measured with a quantitative phase microscope. A diffusion theory was developed for a uniform water medium, and its solution was derived theoretically and verified numerically. The match of the theory in the uniform water medium case was compared to the case of a half-space of glass and a half-space of water, which is used in experiment, and the two cases were found to have qualitative agreement. This diffusion theory was verified experimentally with a photothermal point source, and good agreement was found in the phase curves. The presence of thermal convection in the vertical direction tampers with the amplitude curves, and these results cannot be explained by diffusion alone. A different experimental approach must be used to eliminate this buoyant convective effect, or the photothermal theory must be modified to include convection in the vertical direction. The photothermal wavenumber was estimated by performing a linear fit to the PT phase curves versus radial position at multiple modulation frequencies. With these experimentally determined photothermal wavenumbers, a wavenumber versus modulation frequency curve was plotted and found to be in good agreement with that predicted by thermal diffusion theory for the water medium. The ability of the photothermal imaging method to image cells containing absorptive chemical species was proven by imaging red blood cells with green pumping light. The chemical specificity of the photothermal imaging method was also verified by selectively imaging red blood cells in the presence of a human cheek cell which is

non-absorptive for green light.

Bibliography

[1] L C Aamodt, J C Murphy, and J G Parker. Size considerations in the design of cells for photoacoustic spectroscopy. page 8.

[2] A. C. Boccara, D. Fournier, and J. Badoz. Thermo-optical spectroscopy: Detection by the ''mirage effect''. *Applied Physics Letters*, 36(2):130–132, January 1980.

[3] Ruibo Shang, Shichao Chen, Chengshuai Li, and Yizheng Zhu. Spectral modulation interferometry for quantitative phase imaging. *Biomedical Optics Express*, 6(2):473, February 2015.

[4] Joseph W. Goodman. *Introduction to Fourier Optics*. Roberts and Company Publishers, 2005. Google-Books-ID: ow5xs_Rtt9AC.

[5] G. J. Tearney, R. H. Webb, and B. E. Bouma. Spectrally encoded confocal microscopy. *Optics Letters*, 23(15):1152, August 1998.

[6] James G Fujimoto, Costas Pitris, Stephen A Boppart, and Mark E Brezinski. Optical Coherence Tomography: An Emerging Technology for Biomedical Imaging and Optical Biopsy. *Neoplasia (New York, N.Y.)*, 2(1-2):9–25, January 2000.

[7] F. Vasefi, N. MacKinnon, and D. L. Farkas. Chapter 16 - Hyperspectral and Multispectral Imaging in Dermatology. In Michael R. Hamblin, Pinar Avci, and Gaurav K. Gupta, editors, *Imaging in Dermatology*, pages 187–201. Academic Press, Boston, January 2016.

[8] F. Zernike. Phase contrast, a new method for the microscopic observation of transparent objects part II. *Physica*, 9(10):974–986, December 1942.

[9] S A Latt, G Stetten, L A Juergens, H F Willard, and C D Scher. Recent developments in the detection of deoxyribonucleic acid synthesis by 33258 Hoechst fluorescence. *Journal of Histochemistry & Cytochemistry*, 23(7):493–505, July 1975. Publisher: Journal of Histochemistry & Cytochemistry.

[10] Kapuscinski J. DAPI: a DNA-specific fluorescent probe. *Biotechnic & histochemistry : official publication of the Biological Stain Commission*, 70(5):220–33, 1995.

[11] Ashwinkumar Bhirde, Jin Xie, Maggie Swierczewska, and Xiaoyuan Chen. Nanoparticles for cell labeling. *Nanoscale*, 3(1):142–153, January 2011.

[12] Joowon Lim, Ahmed B. Ayoub, Elizabeth E. Antoine, and Demetri Psaltis. High-fidelity optical diffraction tomography of multiple scattering samples. *Light: Science & Applications*, 8(1):82, September 2019. Number: 1 Publisher: Nature Publishing Group.

[13] Luca Quaroni and Theodora Zlateva. Infrared spectromicroscopy of biochemistry in functional single cells. *Analyst*, 136(16):3219–3232, July 2011. Publisher: The Royal Society of Chemistry.

[14] D. P. Almond, Pravin Patel, and P. M. Patel. *Photothermal Science and Techniques*. Springer Science & Business Media, May 1996. Google-Books-ID: ziY04xpnekUC.

[15] Susana Novais, Marta S. Ferreira, and João L. Pinto. Determination of thermo-optic coefficient of ethanol-water mixtures with optical fiber tip sensor. *Optical Fiber Technology*, 45:276–279, November 2018.

[16] Stephen E. Bialkowski. *Photothermal Spectroscopy Methods for Chemical Analysis*. John Wiley & Sons, January 1996. Google-Books-ID: 2F83tQEACAAJ.

[17] Horatio Scott Carslaw and John Conrad Jaeger. *Conduction of Heat in Solids*. Clarendon Press, 1986. Google-Books-ID: y20sAAAAYAAJ.

[18] Allan Rosencwaig and Allen Gersho. Theory of the photoacoustic effect with solids. *Journal of Applied Physics*, 47(1):64–69, January 1976. Publisher: American Institute of Physics.

[19] Grover C. Wetsel Jr and F. Alan McDonald. Subsurface-structure determination using photothermal laser-beam deflection. *Applied Physics Letters*, 41(10):926, August 1998. Publisher: American Institute of PhysicsAIP.

[20] Allan Rosencwaig, Jon Opsal, W L Smith, and D L Willenborg. Detection of thermal waves through optical reflectance. page 4.

[21] C. Eggeling, J. Widengren, R. Rigler, and C. A. M. Seidel. Photobleaching of Fluorescent Dyes under Conditions Used for Single-Molecule Detection: Evidence of Two-Step Photolysis. *Analytical Chemistry*, 70(13):2651–2659, July 1998. Publisher: American Chemical Society.

[22] Stéphane Berciaud, Laurent Cognet, Gerhard A. Blab, and Brahim Lounis. Photothermal Heterodyne Imaging of Individual Nonfluorescent Nanoclusters and Nanocrystals. *Physical Review Letters*, 93(25):257402, December 2004.

[23] V.P. Zharov and D.O. Lapotko. Photothermal imaging of nanoparticles and cells. *IEEE Journal of Selected Topics in Quantum Electronics*, 11(4):733–751, July 2005. Conference Name: IEEE Journal of Selected Topics in Quantum Electronics.

[24] Guillaume Baffou, Pierre Bon, Julien Savatier, Julien Polleux, Min Zhu, Marine Merlin, Hervé Rigneault, and Serge Monneret. Thermal Imaging of Nanostructures by Quantitative Optical Phase Analysis. *ACS Nano*, 6(3):2452–2458, March 2012.

[25] C. Li, S. Chen, and Y. Zhu. Maximum Likelihood Estimation of Optical Path Length in Spectral Interferometry. *Journal of Lightwave Technology*, 35(22):4880–4887, November 2017. Conference Name: Journal of Lightwave Technology.

[26] John C. Strikwerda. *Finite Difference Schemes and Partial Differential Equations, Second Edition*. Other Titles in Applied Mathematics. Society for Industrial and Applied Mathematics, January 2004.